



## On recovering distributed IP information from inductive source time domain electromagnetic data

Journal:	<i>Geophysical Journal International</i>
Manuscript ID:	GJI-S-15-0747
Manuscript Type:	Research Paper
Date Submitted by the Author:	03-Sep-2015
Complete List of Authors:	KANG, SEOGI; University of British Columbia, Earth, Ocean and Atmospheric Sceince Oldenburg, Doug; University of British Columbia, Earth, Ocean and Atmospheric Sceince
Keywords:	Electrical properties < GEOMAGNETISM and ELECTROMAGNETISM, Geomagnetic induction < GEOMAGNETISM and ELECTROMAGNETISM, Inverse theory < GEOPHYSICAL METHODS, Numerical approximations and analysis < GEOPHYSICAL METHODS

SCHOLARONE™  
Manuscripts

1  
2  
3 submitted to *Geophys. J. Int.*  
4  
5  
6  
7  
8

# 9 On recovering distributed IP information from inductive 10 11 source time domain electromagnetic data 12 13

14  
15  
16  
17 Seogi Kang and Douglas W. Oldenburg  
18  
19

20 *Department of Earth, Ocean and Atmospheric Sciences, University of British Columbia, B.C. V6T 1Z4, Canada*  
21  
22  
23  
24  
25

## 26 SUMMARY 27

28 We develop a procedure to invert time domain induced polarization (IP) data for inductive  
29 sources. Our approach is based upon the inversion methodology in electrical IP (EIP),  
30 which uses a linear sensitivity function that is independent of time. However significant  
31 modifications are required for inductive source IP (ISIP), because electric fields in the  
32 ground do not achieve a steady state. The time history for these fields need to be evaluated  
33 and then used to define approximate IP currents. The resultant data, either a magnetic field  
34 or its derivative, is evaluated through the Biot-Savart law. This forms the desired linear re-  
35 lationship between data and pseudo-chargeability. Our inversion procedure has three fol-  
36 lowing steps: 1) Invert TEM data and recover 3D distribution of conductivity. 2) Decouple  
37 IP responses embedded in the observations by forward modelling the TEM data due to a  
38 background conductivity and subtract these from the observations. 3) Use the linearized  
39 sensitivity function to invert data at each time channel and recover pseudo-chargeability.  
40 Post-interpretation of the recovered pseudo-chargeabilities at multiple times allows re-  
41 covery of intrinsic Cole-Cole parameters such as time constant and chargeability. The  
42 procedure is applicable to all inductive source survey geometries but we focus upon air-  
43 borne time domain EM (ATEM) data with a coincident-loop configuration because of  
44 the distinctive negative IP signal that is observed over a chargeable body. Numerous as-  
45 sumptions are adopted to generate our linearized modelling but we systematically test the  
46  
47  
48  
49  
50  
51  
52  
53  
54  
55  
56  
57  
58  
59  
60

1  
2    2 *Seogi Kang and Douglas W. Oldenburg*  
3  
4  
5  
6  
7  
8  
9  
10  
11  
12  
13  
14  
15  
16  
17  
18

19  
20  
21  
22  
23  
24  
25  
26  
27  
28  
29  
30  
31  
32  
33  
34  
35  
36  
37  
38  
39  
40  
41  
42  
43  
44  
45  
46  
47  
48  
49  
50  
51  
52  
53  
54  
55  
56  
57  
58  
59  
60

capability and accuracy of the linearization for ISIP responses for different conductivity structures. On test examples we show: (a) our decoupling procedure enhances the ability to extract information about existence and location of chargeable targets directly from the data maps; (b) the horizontal location of a target body can be well recovered; (c) the overall geometry of a target body might be recovered but much of that inference requires a depth weighting to be included; (d) we can recover estimates of intrinsic  $\tau$  and  $\eta$  that may be useful for distinguishing between two chargeable targets.

## 1 1 INTRODUCTION

2 The electrical conductivity of earth materials can be frequency dependent with the effective conductivity decreasing with decreasing frequency due to the buildup of electric charges that occur under the application of an electric field. Effectively, the rock is electrically polarized. Applications of induced polarization (IP) surveys to find chargeable material have been particularly successful in mineral exploration for disseminated sulphide or porphyry deposits (Pelton et al. 1978; Fink et al. 1990) and also in geotechnical and environmental problems (Kemna et al. 2012).

3 Polarization charges can accumulate whenever there is an electric field in a medium. In controlled source surveys, the transmitter can be a galvanic source (a generator attached to two grounded electrodes), or an inductive source (arising from currents flowing in a wire loop). Most research and application has focused upon using grounded electrodes and measuring electric fields; this is called an EIP survey (Seigel 1959). Magnetic fields arising from polarization currents (MIP survey) have also been successfully used, particularly in mineral exploration geologies characterized by a conductive overburden (Seigel 1974). In recent years attention has also turned towards the use of inductive sources. Inductive source IP (ISIP), can have transmitters in the air or on the ground and the waveforms can be in either the frequency or time domain. Recently (Marchant et al. 2012) showed how, by collecting data at two frequencies, it was possible to measure data that depended purely on IP signals and that these data can be inverted to recover a 3D distribution of chargeability. For time domain systems the observations of negative transients in coincident loop systems provide an distinctive verification of the existence of chargeable material (Weidelt 1982). These negative transients have been frequently observed (Smith & Klein 1996; Kang & W. Oldenburg 2015). The effects of chargeable objects on time domain system with inductive sources have been carefully investigated (Smith et al. 1988; Flis et al. 1989; ElKalioubey & Eldiwany 2004; Marchant et al. 2014) and approximate interpretation tools

1  
2  
3       *On recovering distributed IP information from inductive source time domain electromagnetic data*    3  
4  
56       (Kratzer & Macnae 2012; Hodges & Chen 2014; Kwan et al. 2015) are being developed. The ability  
7       to fully invert these data in 3D is still lacking.  
89       Extracting information about the complex conductivity can be done in a variety of ways. In prin-  
10       ciple it can be solved by finding a function  $\sigma(x, y, z, \omega)$  or parameterizing the complex conductivity,  
11       usually with a Cole-Cole type model, and finding the distribution of those parameters (Fiandaca et al.  
12       2012; Marchant et al. 2013; Xu & Zhdanov 2015). Traditionally, however, with EIP and time do-  
13       main waveforms, one first estimates the background conductivity from the asymptotic on-time data  
14       and then inverts off-time data to recover information about “chargeability” (Oldenburg & Li 1994).  
15       This is carried out by solving an inverse problem using a linear function where the sensitivities de-  
16       pend upon geometry of the survey and the background conductivity. The recovered values are really  
17       pseudo-chargeability, and they have the same units as the data (eg. msec, mV/V). The same procedure  
18       can be used in frequency domain experiments but the data might have units of mrad and pfe (percent  
19       frequency effect). Inversion of IP data to recover 2D or 3D distributions of pseudo-chargeability are  
20       now commonly carried out (Kemna et al. 2012). These inversions delineate locations of high pseudo-  
21       chargeability and the geometry of the bodies. MIP data can be inverted with the same methodology  
22       (Chen & W. Oldenburg 2003).  
23  
2425       The physical mechanisms by which polarization charges and currents are established in the ground  
26       are independent of the type of transmitter and waveform; the important quantity is the time history of  
27       the electric field within the earth. The challenge posed by the use of inductive sources is that steady  
28       state electric fields are not established inside the earth as they are for EIP or MIP surveys. At any  
29       location in the earth the electric field will increase to a maximum value and then decrease as the  
30       electromagnetic (EM) wave diffuses through. The EM fields at any position and time depend upon the  
31       convolution of the electric field with the time-dependent conductivity of the rock. Unravelling these  
32       complexities, and providing a framework for extracting information about IP characteristics of rocks,  
33       are issues we address in our paper.  
3435       Our procedure involves three principal steps: 1) estimating the 3D background conductivity and  
36       carrying out an EM decoupling to produce IP data ( $d^{IP}$ ), and 2) developing a linearized formulation  
37       using the Biot-Savart law and an effective pseudo-chargeability that encapsulates time dependencies  
38       of the EM fields at any location in the earth, 3) inverting  $d^{IP}$  using the linear functional to recover  
39       pseudo-chargeability at each time channel, and subsequently processing these multi-channel data to  
40       obtain information about Cole-Cole parameters for each point in the subsurface. Each of these steps  
41       requires special attention for inductive source data and approximations are required. Our paper pro-  
42       ceeds as follows. We first outline our decomposition process for obtaining  $d^{IP}$  data, define a pseudo-  
43       chargeability, and show how our problem can be linearized. For ATEM surveys with multiple trans-  
44  
45  
46  
47  
48  
49  
50  
51  
52  
53  
54  
55  
56  
57  
58  
59  
60

1  
2  
3 4 *Seogi Kang and Douglas W. Oldenburg*  
5

6 mitters, we show how to generate a single linear inverse problem that can be solved for an effective  
7 pseudo-chargeability. The data and pseudo-chargeability are linearly related through the Biot-Savart  
8 law and hence a depth weighting, required for other potential field inversions, is necessary to obtain  
9 geologic solutions. The inversion can be carried out at multiple times and a pseudo-chargeability as a  
10 function of time can be generated. These results can be used to recover intrinsic decays of the charge-  
11 able rock units and thus potentially differentiate between rock types in the same manner as carried  
12 out by Yuval & Oldenburg (1997) using EIP data. In our numerical experiments, we investigate the  
13 above steps and procedures, test our assumptions, and evaluate the circumstances under which our  
14 technique might provide meaningful results. Although we focus upon airborne TEM data, the anal-  
15 ysis we present here is valid for surveys on the earth's surface using inductive sources and also for  
16 grounded sources although many of the complications we deal with are not relevant.  
17  
18  
19  
20  
21  
22  
23  
24  
25  
26  
27  
28  
29  
30  
31  
32  
33  
34  
35  
36  
37  
38  
39  
40  
41  
42  
43  
44  
45  
46  
47  
48  
49  
50  
51  
52  
53  
54  
55  
56  
57  
58  
59  
60

## 2 COMPLEX CONDUCTIVITY

An often-used representation for complex conductivity in the frequency domain is the Cole-Cole model (Cole & Cole 1941):

$$\sigma(\omega) = \sigma_\infty - \sigma_\infty \frac{\eta}{1 + (1 - \eta)(i\omega\tau)^c} = \sigma_\infty + \Delta\sigma(\omega), \quad (1)$$

where  $\sigma_\infty$  is the conductivity at infinite frequency,  $\eta$  is the intrinsic chargeability,  $\tau$  is the time constant and  $c$  is the frequency dependency. Real and imaginary parts of complex conductivity in frequency domain are shown in Fig. 1(a) with Cole-Cole parameters:  $\sigma_\infty = 10^{-2}$  S/m,  $\eta = 0.5$ ,  $\tau = 0.01$ , and  $c=1$ . By applying inverse Fourier transform with time dependency,  $e^{i\omega t}$ , we have

$$\sigma(t) = \mathcal{F}^{-1}[\sigma(\omega)] = \sigma_\infty\delta(t) + \Delta\sigma(t), \quad (2)$$

where  $\delta(t)$  is Dirac delta function, and  $\mathcal{F}^{-1}[\cdot]$  is inverse Fourier transform operator. Note that we only deal with causal function, which is defined when  $t \geq 0$ . We rewrite  $\Delta\sigma(t)$  as

$$\Delta\sigma(t) = -\sigma_\infty\tilde{\eta}^I(t), \quad (3)$$

where intrinsic pseudo-chargeability,  $\tilde{\eta}^I(t)$  is defined as

$$\tilde{\eta}^I(t) = -\frac{\Delta\sigma(t)}{\sigma_\infty}. \quad (4)$$

Cole-Cole model in time domain is also shown in Fig. 1(b). Used Cole-Cole parameters here are same as the above.

1  
2  
3      *On recovering distributed IP information from inductive source time domain electromagnetic data*    5  
4  
5

6      **3 DECOMPOSITION OF OBSERVED RESPONSES**  
7  
8

9      IP effects in the observed data are coupled with EM effects. We need to decompose the observations  
10 to isolate data associated only with the IP phenomena. Maxwell's equations in the time domain, with  
11 a quasi-static approximation, are written as:  
12

$$13 \quad \vec{\nabla} \times \vec{e} = -\frac{\partial \vec{b}}{\partial t}, \quad (5)$$

$$16 \quad \vec{\nabla} \times \frac{1}{\mu} \vec{b} - \vec{j} = \vec{j}_s, \quad (6)$$

17      where  $\vec{e}$  is the electric field ( $V/m$ ),  $\vec{b}$  is the magnetic flux density ( $Wb/m^2$ ),  $\vec{j}_s$  is the current source  
18 ( $A/m^2$ ) and  $\mu$  is the magnetic permeability ( $H/m$ ). Here  $\vec{j}$  is the conduction current ( $A/m^2$ ). In  
19 the frequency domain, this conduction current,  $\vec{J}$  is related to conductivity via Ohms law:  $\vec{J}(\omega) =$   
20  $\sigma(\omega) \vec{E}(\omega)$  where  $\vec{E}$  is the electric field. Converting this relationship to time domain using the inverse  
21 Fourier transform yields:  
22

$$23 \quad \vec{j}(t) = \sigma(t) \otimes \vec{e}(t) = \int_0^t \sigma(u) e(t-u) du. \quad (7)$$

24      where  $\otimes$  indicates time convolution for a causal signal. Thus the current density depends upon the  
25 previous history of the electric field. As in Smith et al. (1988), we represent total fields as  $\vec{e} = \vec{e}^F + \vec{e}^{IP}$ ,  
26  $\vec{b} = \vec{b}^F + \vec{b}^{IP}$  and  $\vec{j} = \vec{j}^F + \vec{j}^{IP}$ , where superscript  $F$  indicates fundamental and  $IP$  is induced  
27 polarization. Here fundamental fields indicate EM fields without IP effects. Substituting into eqs (5)  
28 and (6) yields the following sequences:  
29

$$30 \quad \vec{\nabla} \times (\vec{e}^F + \vec{e}^{IP}) = -\frac{\partial}{\partial t} (\vec{b}^F + \vec{b}^{IP}), \quad (8)$$

$$31 \quad \vec{\nabla} \times \frac{1}{\mu} (\vec{b}^F + \vec{b}^{IP}) - (\vec{j}^F + \vec{j}^{IP}) = \vec{j}_s. \quad (9)$$

32      The fundamental equations can be written as  
33

$$34 \quad \vec{\nabla} \times \vec{e}^F = -\frac{\partial \vec{b}^F}{\partial t}, \quad (10)$$

$$35 \quad \vec{\nabla} \times \frac{1}{\mu} \vec{b}^F - \vec{j}^F = \vec{j}_s. \quad (11)$$

36      Here  
37

$$38 \quad \vec{j}^F = \sigma_\infty \vec{e}^F. \quad (12)$$

39      Substituting the fundamental fields into eqs (5) and (6) yields the expressions for the IP fields  
40

$$41 \quad \vec{\nabla} \times \vec{e}^{IP} = -\frac{\partial \vec{b}^{IP}}{\partial t}, \quad (13)$$

$$42 \quad \vec{\nabla} \times \frac{1}{\mu} \vec{b}^{IP} = \vec{j}^{IP}. \quad (14)$$

1  
2  
3     6     *Seogi Kang and Douglas W. Oldenburg*  
4  
5

6     Let  $F[\cdot]$  denote operator associated with Maxwell's equations, and let  $d$  denote the observations  
7     that include both EM and IP effects. Keeping the same notation, we can obtain  $d = d^F + d^{IP}$ , where  
8      $d^F$  and  $d^{IP}$  are fundamental and IP responses, respectively. Based on this, we define the IP datum as  
9  
10

$$11 \quad d^{IP} = d - d^F = F[\sigma(t)] - F[\sigma_\infty]. \quad (15)$$

12  
13     4     Here  $F[\sigma_\infty]$  corresponds to the fundamental response ( $d^F$ ). This subtraction process acts as an EM  
14     5     decoupling process, which removes the EM effects from the measured responses. This is the same  
15     6     procedure that formed the basis of work by Routh & Oldenburg (2001).  
16  
17

18  
19     7     **4 PSEUDO-CHARGEABILITY FOR INDUCTIVE SOURCES**  
20

21     8     Combining eqs (2) and (7) writing  $\vec{j}(t) = \vec{j}^F + \vec{j}^{IP}$  we obtain  
22

$$23 \quad \vec{j}^{IP} = \sigma_\infty \vec{e}^{IP} + \vec{j}^{pol}, \quad (16)$$

24     9     where the polarization current ( $\vec{j}^{pol}$ ) is  
25  
26

$$27 \quad \vec{j}^{pol}(t) = \Delta\sigma(t) \otimes \vec{e}(t). \quad (17)$$

28  
29     10     If the electric field has different characteristics for the inductive and galvanic sources this will gen-  
30     11     erate different features in the polarization current. We consider two cases: a) galvanic source without  
31     12     EM induction and b) inductive source with EM induction. The first case corresponds to EIP (Seigel  
32     13     1959), and the second is ISIP. Fig. 2 shows the amplitude of the fundamental electric field ( $\vec{e}^F$ ) in  
33     14     the earth for those two cases. For the galvanic source, the electric field is instantaneous due to the  
34     15     steady-state electric field (Fig. 2 a). However, for the inductive source, the electric field in the off-time  
35     16     is not zero, but increases to a peak and then decays as shown in Fig. 2 (b). The polarization current for  
36     17     the two different sources will be significantly affected by these different electric fields. To capture this  
37     18     difference in a linearized kernel for the IP response, we define pseudo-chargeability ( $\tilde{\eta}(t)$ ) as  
38  
39

$$40 \quad \tilde{\eta}(t) = -\frac{\vec{j}^{pol}(t)}{\vec{j}^{ref}}, \quad (18)$$

41     52     19     where the reference current ( $\vec{j}^{ref}$ ) is defined as  
42  
43

$$44 \quad \vec{j}^{ref} = \sigma_\infty \vec{e}^{ref}. \quad (19)$$

45  
46     56     20     Here  $\vec{e}^{ref}$  is the reference electric field and both  $\vec{j}^{ref}$  and  $\vec{e}^{ref}$  are static fields that are independent  
47     57     21     of time. The pseudo-chargeability defined in eq. (18) is the ratio of the polarization current to the  
48     58     22     reference current. This is a small quantity and it plays an essential role in our linearization.  
49  
50

51     59     23     To evaluate the pseudo-chargeability, we have to identify the reference current or reference electric  
52  
53

3  
4     *On recovering distributed IP information from inductive source time domain electromagnetic data* 75  
6     fields. For the EIP case, the electric field, when there is no IP present, is independent of time as shown  
7     in Fig. 2(a). For the inductive source however, the electric field does not achieve a steady-state, but  
8     increases to a peak then decreases.  
910  
11    Each pixel in the earth has its own reference electric field and time thus both  $\vec{e}^{ref}$  and  $t^{ref}$  have  
12    a 3D distribution. For both EIP and ISIP cases, we mathematically present our choice of the reference  
13    electric field as  
14

15  
16    
$$\vec{e}^{ref} = \vec{e}^F(t) \otimes \delta(t - t^{ref}). \quad (20)$$
  
17

18  
19    The reference time for the EIP case can be any time in the on-time, because the fundamental electric  
20    field for the EIP case does not change in on-time.  
2122    By rearranging eq. (18), we obtain  
23

24  
25    
$$\vec{j}^{pol} = -\vec{j}^{ref} \tilde{\eta}(t). \quad (21)$$
  
26

27    This states that the polarization current has an opposite direction to the reference current, and is pro-  
28    portional to the pseudo-chargeability ( $\tilde{\eta}(t)$ ). This conceptual model about the polarization current  
29    shown in eq. (21) is consistent with Seigel (1959)'s result. We note, that for any pixel, even though  
30     $\vec{e}^{ref}$  attains the same value for an ISIP survey as for an EIP survey, the pseudo-chargeability resulting  
31    from an ISIP survey will be less than that from an EIP survey. We can infer from this that linearization  
32    techniques, which have worked so well in EIP problems, should be successful in ISIP problems.  
33  
3435    16    **5 LINEARIZATION**  
36  
3738  
39    Following from the methodologies in EIP, our goal is to express the IP response ( $d^{IP}$ ) as a function  
40    of the pseudo-chargeability ( $\tilde{\eta}(t)$ ) in time  $d^{IP}(t) = J[\tilde{\eta}(t)]$ , where  $J[\cdot]$  is a linear operator which  
41    is independent of time. In doing this we first consider a general EM system which is applicable to  
42    galvanic or inductive sources. For any pixel volume in the earth the amplitude and direction of the  
43    electric field can vary dramatically in time and this results in a complicated IP charging process. If  
44    substantial polarization currents are developed however, they will correspond to a maximum electric  
45    field or reference current aligned in a constant direction. Our formulation focuses on this aspect. We  
46    assume that the final large-scale IP response observed in the data is the result of pixels being charged  
47    with an electric field in a specific direction but with a variable amplitude. Let  $\vec{e}(t)$  be approximated as  
48  
49

50  
51    
$$\vec{e}(t) \approx \vec{e}^{ref} \hat{w}(t), \quad (22)$$
  
52  
53

54    26    where  $\hat{w}(t)$  is defined as:  
55  
56

57  
58    
$$\hat{w}(t) = P_0[w^{ref}(t)]. \quad (23)$$
  
59  
60

1  
2  
3 8 Seogi Kang and Douglas W. Oldenburg  
4  
5

6 Here a projection ( $P_0[\cdot]$ ) of an arbitrary function,  $f(t)$  is  
7  
8

$$P_0[f(t)] = \begin{cases} f(t) & f(t) \geq 0 \\ 0 & \text{if } f(t) < 0, \end{cases} \quad (24)$$

9 and  
10  
11

$$w^{ref}(t) = \frac{\vec{e}^F(t) \cdot \vec{e}^{ref}}{\vec{e}^{ref} \cdot \vec{e}^{ref}}. \quad (25)$$

12 Here  $w^{ref}(t)$  is a dimensionless function that prescribes the time history of the electric field at each  
13 location along the direction of the chosen reference electric field ( $\vec{e}^{ref}$ ). Negative values of  $w^{ref}(t)$   
14 are set to zero in accordance with our conceptual model that polarization currents have an opposite  
15 direction to the reference current (eq. 21). We redefine the pseudo-chargeability as  
16  
17

$$\tilde{\eta}(t) = \tilde{\eta}^I(t) \otimes \hat{w}(t). \quad (26)$$

18 7 The polarization current,  $\vec{j}^{pol}$  can be approximated with eq. (4) as  
19  
20

$$\vec{j}^{pol}(t) \approx -\tilde{\eta}^I(t) \otimes \hat{w}(t) \vec{j}^{ref}. \quad (27)$$

21 8 Substituting this into eq. (16) yields  
22  
23

$$\vec{j}^{IP}(t) \approx \sigma_\infty \vec{e}^{IP}(t) - \tilde{\eta}^I(t) \otimes \hat{w}(t) \vec{j}^{ref} \quad (28)$$

24 9 and this yields  
25  
26

$$\vec{j}^{IP}(t) \approx \sigma_\infty \vec{e}^{IP}(t) - \vec{j}^{ref} \tilde{\eta}(t). \quad (29)$$

27 10 The second term,  $-\vec{j}^{ref} \tilde{\eta}(t)$ , correspond to polarization currents. The first term,  $\sigma_\infty \vec{e}^{IP}(t)$  is  
28 usually omitted (Smith et al. 1988). Here we include it and explore the conditions in which it is  
29 important. Because the reference current is static, any time-dependency in the polarization currents is  
30 encapsulated in the pseudo-chargeability. The buildup and decrease of polarization currents is a slow  
31 process and we assume therefore that this process does not produce induction effects ( $\frac{\partial \vec{b}^{IP}}{\partial t} \approx 0$ ) and  
32 hence we can write  
33  
34

$$\vec{e}^{IP} \approx \vec{e}_{approx}^{IP} = -\vec{\nabla} \phi^{IP}. \quad (30)$$

35 16 By taking the divergence of eq. (29), substituting  $\vec{e}^{IP}$  with eq. (30), and carrying out some linear  
36 algebra, we obtain  
37  
38

$$\phi^{IP}(t) \approx -[\nabla \cdot \sigma_\infty \vec{\nabla}]^{-1} \nabla \cdot \vec{j}^{ref} \tilde{\eta}(t). \quad (31)$$

39 18 By applying the gradient we obtain  
40  
41

$$\vec{e}_{approx}^{IP} = \vec{\nabla} [\nabla \cdot \sigma_\infty \vec{\nabla}]^{-1} \nabla \cdot \vec{j}^{ref} \tilde{\eta}(t). \quad (32)$$

## On recovering distributed IP information from inductive source time domain electromagnetic data 9

1 Thus, the electric field due to the IP effect can be expressed as a function of  $\tilde{\eta}(t)$  in time. This form is  
 2 also applicable to the EIP case.

3 For an inductive source, the data is often either  $\vec{b}$  or its time derivative and hence we also need  
 4 to compute  $\vec{b}^{IP}$  or its time derivative. For this, we first compute  $\vec{j}^{IP}$  then use the Biot-Savart law. By  
 5 substituting eq. (32) into eq. (29), the approximated IP current density,  $\vec{j}_{approx}^{IP}$  can be expressed as

$$14 \quad 15 \quad \vec{j}^{IP}(t) \approx \vec{j}_{approx}^{IP} = \bar{S} \vec{j}^{ref} \tilde{\eta}(t), \quad (33)$$

16 where

$$19 \quad 20 \quad \bar{S} = \sigma_\infty \vec{\nabla} [\nabla \cdot \sigma_\infty \vec{\nabla}]^{-1} \nabla \cdot -\bar{I} \quad (34)$$

21 and  $\bar{I}$  is an identity tensor. Applying the Biot-Savart law we have:

$$23 \quad 24 \quad 25 \quad \vec{b}_{approx}^{IP}(\vec{r}; t) = \frac{\mu_0}{4\pi} \int_{\Omega} \frac{\bar{S} \vec{j}^{ref}(\vec{r}_s) \times \hat{r}}{|\vec{r} - \vec{r}_s|^2} \tilde{\eta}(t) d\vec{r}_s, \quad (35)$$

26 where  $\vec{r}_s$  indicates a vector for a source location, and  $\hat{r} = \frac{\vec{r} - \vec{r}_s}{|\vec{r} - \vec{r}_s|}$ . If  $\sigma_\infty \vec{e}^{IP}$  is omitted in  $\vec{j}^{IP}$  then  
 27 the tensor,  $\bar{S}$  becomes  $-\bar{I}$ . In this situation, the IP current is same as the polarization current, and it  
 28 always has opposite direction to the reference current. This reversed current, along with Biot-Savart  
 29 law, provides a physical understanding about the negative transients in ATEM data when the earth is  
 30 chargeable.

31 Observed data are often the time derivative of  $\vec{b}$ , hence by taking time derivative to the eq. (35),  
 32 we obtain

$$38 \quad 39 \quad 40 \quad -\frac{\partial \vec{b}_{approx}^{IP}}{\partial t}(\vec{r}; t) = \frac{\mu_0}{4\pi} \int_{\Omega} \frac{\bar{S} \vec{j}^{ref}(\vec{r}_s) \times \hat{r}}{|\vec{r} - \vec{r}_s|^2} \left( -\frac{\partial \tilde{\eta}(t)}{\partial t} \right) d\vec{r}_s. \quad (36)$$

41 Here we have chosen to keep the minus signs in eq. (36) so that  $-\frac{\partial \tilde{\eta}(t)}{\partial t}$  is positive when  $\tilde{\eta}(t)$  is  
 42 decaying in time. Accordingly, the IP datum is given by  $-\frac{\partial \vec{b}^{IP}}{\partial t}$ .

43 The IP fields shown in eqs (32), (35) and (36) are linear functionals of  $\tilde{\eta}$  and the equations for a  
 44 single time channel can be discretized in space as

$$48 \quad 49 \quad \mathbf{d}^{IP} = \mathbf{J} \tilde{\eta}, \quad (37)$$

50 where  $\mathbf{J}$  is the corresponding sensitivity matrix. In particular when the observed datum is the time  
 51 derivative of  $\vec{b}$ , the linear relationship can be written as

$$55 \quad 56 \quad \mathbf{d}^{IP} = \mathbf{J} \left( -\frac{\partial \tilde{\eta}}{\partial t} \right). \quad (38)$$

57 A detailed description for the discretization of the linearized kernel is shown in Appendices A and B.

58 The representation in eq. (37) is valid for galvanic and inductive sources but the two assumptions: a)  
 59  $\vec{e} \approx \vec{e}^{ref} \hat{w}(t)$  and b)  $\vec{e}^{IP} \approx -\vec{\nabla} \phi^{IP}$  need to be tested numerically for the case of inductive sources.

1  
2  
3 10 Seogi Kang and Douglas W. Oldenburg  
4  
5

6 1 **IP INVERSION METHODOLOGY**  
7  
8

9 **6.1 3D IP inversion with a linearized kernel**  
10  
11

12 3 The linear inverse problem to recover chargeability is straightforward and is described in Oldenburg  
13 & Li (1994). We rewrite eq. (37) as  
14  
15

$$\mathbf{d}^{pred} = \mathbf{J}\mathbf{m}, \quad (39)$$

16 5 where  $\mathbf{J}$  is the sensitivity matrix of linear problem, which corresponds to  $\mathbf{J}$  shown in eq. (37). Here,  
17 6  $\mathbf{d}^{pred}$  represents IP responses at a single time channel,  $\mathbf{m}$  denotes model parameters, which can be  
18 7 either  $\tilde{\eta}$  or  $-\frac{\partial \tilde{\eta}}{\partial t}$  at the same time. In our work here we invert each time channel of  $d^{IP}$ , separately.  
19  
20

21 8 The solution to the inverse problem is the model  $\mathbf{m}$  that solves the optimization problem  
22  
23

$$\text{minimize } \phi = \phi_d(\mathbf{m}) + \beta \phi_m(\mathbf{m}) \text{ s.t. } 0 \leq \mathbf{m}, \quad (40)$$

24 9 where  $\phi_d$  is a measure of data misfit,  $\phi_m$  is a user-defined model objective function and  $\beta$  is regular-  
25 10 ization or trade-off parameter. We solve this optimization problem using a projected Gauss-Newton  
26 11 method (Kelley 1999). The value of  $\beta$  is determined using a cooling technique where  $\beta$  is progres-  
27 12 sively reduced from some high value. The inversion is stopped when the tolerance is reached (cf.  
28 13 Oldenburg & Li (2005); Kang et al. (2014)).  
29  
30

31 14 We use the sum of the squares to measure data misfit  
32  
33

$$\phi_d = \|\mathbf{W}_d(\mathbf{A}\mathbf{m} - \mathbf{d}^{obs})\|_2^2 = \sum_{j=1}^N \left( \frac{\mathbf{d}_j^{pred} - \mathbf{d}_j^{obs}}{\epsilon_j} \right)^2, \quad (41)$$

34 15 where  $N$  is the number of the observed data and  $\mathbf{W}_d$  is a diagonal data weighting matrix which  
35 16 contains the reciprocal of the estimated uncertainty of each datum ( $\epsilon_j$ ) on the main diagonal,  $\mathbf{d}^{obs}$  is  
36 17 a vector containing the observed data,  $\mathbf{d}^{pred}$  is a vector containing calculated data from a linear eq.  
37 18 given in eq. (39). The model objective function,  $\phi_m$ , is a measure of the amount structure in the model  
38 19 and upon minimization this will generate a smooth model which is close to a reference model,  $\mathbf{m}_{ref}$ .  
39  
40

41 20 We define  $\phi_m$  as  
42  
43

$$\phi_m = \sum_{i=s,x,y,z} \alpha_i \|\mathbf{W}_i \mathbf{W}(\mathbf{m} - \mathbf{m}_{ref})\|_2^2, \quad (42)$$

44 21 where  $\mathbf{W}_s$  is a diagonal matrix, and  $\mathbf{W}_x$ ,  $\mathbf{W}_y$  and  $\mathbf{W}_z$  are discrete approximations of the first deriva-  
45 22 tive operator in  $x$ ,  $y$  and  $z$  directions, respectively. The  $\alpha$ 's are weighting parameters that balance the  
46 23 relative importance of producing small or smooth models.  
47  
48

49 24 Because we are inverting each time channel of  $d^{IP}$  datum, separately, we may not have intrinsic  
50 25 depth resolution. This could be overcome if there were multiple receivers for each transmitter, although  
51 26 usual ATEM surveys only have a single receiver. To compensate for this, and similar to the magnetic  
52  
53

1  
2  
3      *On recovering distributed IP information from inductive source time domain electromagnetic data* 11  
4  
5

6      inversion (Li & Oldenburg 1996), we apply a depth weighting through model weighting matrix ( $\mathbf{W}$ ):  
7  
8

$$\mathbf{W} = \text{diag}(\mathbf{z} - \mathbf{z}_0)^{1.5}, \quad (43)$$

9      where  $\mathbf{z}$  and  $\mathbf{z}_0$  are discretized depth locations and reference depth in the 3D domain. For the imple-  
10  
11  
12  
13  
14  
mentation of our IP inversion algorithm, we use an open source python package for simulation and  
gradient-based parameter estimation in geophysics called SIMPEG (Cockett et al. 2015).  
15  
16

17      **6.2 Extracting intrinsic IP parameters**  
18

19      The output of our IP inversion is a 3D distribution of the pseudo-chargeability at multiple time chan-  
20  
21  
22  
23  
nels. As its name suggests, pseudo-chargeability is not an intrinsic IP parameter like chargeability, but  
it is a convoluted property between  $\tilde{\eta}^I(t)$  and  $\hat{w}(t)$ :  
24  
25

$$\tilde{\eta}(t) = \tilde{\eta}^I(t) \otimes \hat{w}(t), \quad (44)$$

26  
27      with the definition of intrinsic pseudo-chargeability (eq. 4). We would now like to use the  $\tilde{\eta}(t)$  as the  
28  
29  
30  
31  
data and recover intrinsic parameters such as  $\eta, \tau, c$  in a Cole-Cole model. Assuming a Debye model  
( $c=1$ ), we obtain  
32  
33

$$\tilde{\eta}^I(t) = \frac{\eta}{(1-\eta)\tau} e^{-\frac{t}{(1-\eta)\tau}}, \quad (45)$$

34  
35      Since we have  $\sigma_\infty$  we can compute  $\hat{w}(t)$ , which is the time history of the electric field. Accord-  
36  
37  
38  
39  
40  
41  
ingly, we can unravel the recovered pseudo-chargeability to extract intrinsic IP parameters such as  
chargeability( $\eta$ ) and time constant ( $\tau$ ). We use a gradient-based optimization and thus we need the  
sensitivity function for the pseudo-chargeability (eq. 44) with respect to  $\eta$  and  $\tau$ . To simplify this  
procedure, we rewrite intrinsic pseudo-chargeability as  
42  
43

$$\tilde{\eta}^I(t) = ae^{-bt}, \quad (46)$$

44  
45      where  $a = \frac{\eta}{(1-\eta)\tau}$  and  $b = \frac{1}{(1-\eta)\tau}$ . Then we take derivative of  $\tilde{\eta}(t)$  with regard to  $a$  and  $b$ :  
46  
47

$$\frac{\partial \tilde{\eta}(t)}{\partial a} = e^{-bt} \otimes \hat{w}(t), \quad (47)$$

$$\frac{\partial \tilde{\eta}(t)}{\partial b} = -ate^{-bt} \otimes \hat{w}(t). \quad (48)$$

53  
54      With these sensitivity functions, we can set up an inverse problem, and recover  $a$  and  $b$ . Chargeability  
55  
56  
and time constant can be obtained by using  $a$  and  $b$ :  
57  
58

$$\eta = \frac{a}{b}, \quad (49)$$

$$\tau = \frac{1}{(1-a/b)b}. \quad (50)$$

1  
2  
3 12 *Seogi Kang and Douglas W. Oldenburg*  
4  
5

6 We apply this inversion separately to each cell in the recovered pseudo-chargeability in a manner  
7 similar to (Yuval & Oldenburg 1997). For the better representation of time-dependent conductivity, a  
8 different parameterization such as stretched-exponential (Kohlrausch 1854) or Cole-Cole model with  
9 variable  $c$  can be implemented.  
10  
11

12 13 5 **6.3 Handling multiple transmitters in ATEM surveys**  
14  
15

16 The work for inductive sources in the previous sections has been developed for a single transmitter  
17 and 3D information about chargeability can be obtained if there are multiple receivers. For ATEM data  
18 however, we have only a single receiver location for each transmitter but we have multiple transmitter  
19 locations. Our goal is to alter the problem to work with an effective pseudo-chargeability.  
20  
21

22 In our linearized eq. (37), each transmitter has its own sensitivity and pseudo-chargeability. For our  
23 airborne case the sensitivity for the  $k$ -th transmitter is the  $k$ -th row of  $\mathbf{J}$  and the pseudo-chargeability  
24 is  $\tilde{\eta}^k$ . The corresponding IP datum is  
25  
26

$$27 \quad d_k^{IP}(t) = \sum_{i=1}^{nC} J_{k,i} \tilde{\eta}_i^k(t), \quad k = 1, \dots, nTx, \quad (51)$$

28 where  $nTx$  is the number of transmitters,  $nC$  is the number of cells in the domain, and  $J_{k,i}$  indicates  
29 an element of the Jacobian matrix for the  $k$ -th transmitter and the  $i$ -th cell. We want to replace  $\tilde{\eta}_i^k$  with  
30 a single effective pseudo-chargeability  $\tilde{\eta}^k$  and therefore write the IP datum as  
31  
32

$$33 \quad d_k^{IP}(t) = \sum_{i=1}^{nC} J_{k,i} \tilde{\eta}_i(t), \quad k = 1, \dots, nTx, \quad (52)$$

34 The waveforms are different for each transmitter and hence this representation cannot be exact. To  
35 examine the implications of this it suffices to look at the contribution of any volumetric pixel. Each  
36 pixel contributes to all of the IP data but in differing amounts. The total contribution of the  $i$ -th pixel  
37 to the  $nTx$  data set at a single time is  
38  
39

$$40 \quad q_i = \sum_{k=1}^{nTx} J_{k,i} \tilde{\eta}_i^k(t), \quad i = 1, \dots, nC. \quad (53)$$

41 Our goal is to find an effective chargeability that produces the same net effect on the measured data.  
42  
43 20 We search for a transmitter-independent  $\tilde{\eta}_i$  such that  
44  
45

$$46 \quad q_i^{est} = \sum_{k=1}^{nTx} J_{k,i} \tilde{\eta}_i(t), \quad i = 1, \dots, nC. \quad (54)$$

47  
48 22 Minimizing the least squares difference between eqs (53) and (54) yields  
49  
50

$$51 \quad \tilde{\eta}_i(t) = \frac{\sum_{k=1}^{nTx} J_{k,i}^2 \tilde{\eta}_i^k(t)}{\sum_{k=1}^{nTx} J_{k,i}^2} = \sum_{k=1}^{nTx} a_i^k \tilde{\eta}_i^k(t), \quad i = 1, \dots, nC. \quad (55)$$

1  
2  
3      *On recovering distributed IP information from inductive source time domain electromagnetic data*    13  
4  
5

6      where normalized weight ( $a_i^k$ ) is  
7  
8

$$a_i^k = \frac{J_{k,i}^2}{\sum_{k=1}^{nTx} J_{k,i}^2}, \quad i = 1, \dots, nC. \quad (56)$$

9  
10      With the above understanding about how  $\tilde{\eta}_i$  relates to the  $\tilde{\eta}_i^k$  from each transmitter we can proceed  
11  
12      as follows. Firstly, from eq. (26) we have  
13

14  
15       $\tilde{\eta}_i^k(t) = \tilde{\eta}^I \otimes \hat{w}_i^k(t) \quad (57)$   
16

17      Substituting eqs (57) into (55) allows us to write  
18

19  
20       $\tilde{\eta}_i(t) = \tilde{\eta}^I(t) \otimes w_i^e(t), \quad (58)$   
21

22      where we define effective time history of the electric field,  $w_i^e(t)$  as  
23  
24

$$w_i^e(t) = \sum_{k=1}^{nTx} a_i^k \hat{w}_i^k(t), \quad i = 1, \dots, nC. \quad (59)$$

25      The above equations shows that the pseudo-chargeability for any pixel recovered from the inversion  
26  
27      is equal to the convolution of the intrinsic pseudo-chargeability ( $\tilde{\eta}^I(t)$ ) with an effective time history  
28  
29      of the electric field ( $w^e(t)$ ). Although it is somewhat involved, the  $w^e(t)$  associated with each pixel can  
30  
31      be evaluated by knowing the electric fields associated with the fundamental EM problem. Ultimately  
32  
33      this allows us to estimate the parameters associated with the intrinsic pseudo-chargeability in the same  
34  
35      manner as outlined for the case with a single transmitter. Our ability to evaluate the  $w^e(t)$  and test the  
36  
37      validity of eq. (52) will be treated in Section 7.5.

38  
39      **6.4 IP inversion procedure**  
40

41      As seen in the previous sections the extraction of IP information from TEM data has multiple steps.  
42  
43      These include: (1) invert TEM data and recover a 3D conductivity model ( $\sigma_{est}$ ). (2) Forward model  
44  
45       $\sigma_{est}$  to obtain the fundamental response  $d^F$  and subtract it from the observations to obtain  $d^{IP}$  data.  
46  
47      (3) Invert  $d^{IP}$  data to recover pseudo-chargeability model at individual time channels using the rela-  
48  
49      tionship in eq. (37). (4) Further, process the inversion outputs at multiple time-channels to estimate  
50  
51      the Cole-Cole, or equivalent IP parameters.

52      In the following we investigate each of the above steps via numerical simulations and test the  
53  
54      validity of our assumptions.

55  
56      **7 NUMERICAL EXPERIMENTS**  
57

58  
59      For our numerical experiments we concentrate upon coincident loop ATEM surveys. This choice is  
60  
61      made because of the observed negative transients that are direct indicators of IP phenomena (Kratzer

1  
2  
3 14 *Seogi Kang and Douglas W. Oldenburg*  
4  
5

6 & Macnae 2012; Kang & W. Oldenburg 2015; Kang et al. 2015), and the extensive use of this survey  
7 by industry.  
8

9 We begin with a simple IP model composed of a chargeable block in a half-space as shown in  
10 Figure 3. Cole-Cole parameters of the block are  $\eta = 0.2$ ,  $\tau = 0.005$  and  $c = 1$ . The conductivity of the  
11 half-space,  $(\sigma_1)$  is  $10^{-3}$  S/m, whereas  $\sigma_2$ , the conductivity at infinite frequency,  $\sigma_\infty$ , for the chargeable  
12 body, is variable. We consider three cases: a) canonical ( $\sigma_2 = \sigma_1$ ), b) conductive ( $\sigma_2 = 10^2 \times \sigma_1$ ) and  
13 c) resistive models ( $\sigma_2 = 10^{-2} \times \sigma_1$ ). The 3D earth is discretized with  $50 \times 50 \times 50$  m core cells and the  
14 number of cells in the domain is  $41 \times 41 \times 40$ . The size of the chargeable body is  $250 \times 250 \times 200$  m and  
15 the top boundary is located 50 m below the surface. The EMTDIP code (Marchant et al. 2014) is used  
16 to compute forward ATEM responses that include IP effects. The survey consisting of 11 soundings  
17 along each of 11 lines is shown in Fig. 3(a). Data are from a coincident-loop system and both Tx and  
18 Rx are located 30 m above the surface; the radius of the loop is 10 m. A step-off transmitter waveform  
19 is used and the range of the observed time channels is 0.01-60 ms. The observed responses can be the  
20 vertical component of  $\vec{b}$  or  $\frac{\partial \vec{b}}{\partial t}$ .  
21  
22

23 In this section, we first decompose the observed responses and the total currents into funda-  
24 mental and IP portions to aid in the basic understanding of IP effects in ATEM data. Second, we  
25 validate the linearized functional by computing the approximate IP current and IP responses, and  
26 compare these with the true values. Third, we investigate the feasibility of detecting an effective  
27 pseudo-chargeability in 3D IP inversion when multi-transmitters are used. Fourth, we invert the IP  
28 data and recover 3D distributions of pseudo-chargeability at multiple times. Lastly, we use the recov-  
29 ered pseudo-chargeabilities to examine the potential to extract intrinsic Cole-Cole parameters.  
30  
31

## 32 7.1 IP responses 33

34 Using the EMTDIP code and carrying out two simulations, we compute the IP data via subtraction in  
35 eq. (15). Fig. 4 shows the observed, fundamental, and IP responses at a sounding location above the  
36 center of the chargeable body for (a) canonical, (b) conductive and (c) resistive models. Both  $b_z$  and  
37  $-\frac{\partial b_z}{\partial t}$  data are shown. The IP effects are most noticeable for the conductive body and we turn attention  
38 to this example first. The IP response starts to significantly affect the observations near 0.6 ms and the  
39 observed responses show a sign reversal near 1 ms. Beyond that time the signal is dominated by the IP.  
40 The dashed line in Fig. 4(b) shows that after turning off the transmitter current, the IP current increases  
41 (as inferred by the magnitude of the  $b_z$  field) until about 1 ms and then decreases. We interpret this  
42 in terms of charging and discharging phases and a vertical dashed line in the figure defines the two  
43 phases. In the charging phase at early times the EM effects dominate and IP signals are not expected  
44 to be observed. In the discharging phase, which occurs at later time, the IP effects may eventually  
45

1  
2  
3     *On recovering distributed IP information from inductive source time domain electromagnetic data* 15  
4  
56     1 dominate the EM effects. The maximum of the  $b_z^{IP}$  corresponds to the zero crossing for  $\frac{\partial b_z^{IP}}{\partial t}$  but  
7     2 the times at which the IP signal becomes dominant are delayed compared to  $b_z^{IP}$ . By comparing the  
8     3 observations with the fundamental fields we see that the IP signal could be recognized in the  $b_z$  data  
9     4 near 0.7 ms and near 2.0 ms in the  $\frac{\partial b_z}{\partial t}$  data.  
10  
11  
1213     5 The plots for the canonical and resistive bodies show that the time that separates charging and  
14     6 discharging occurs earlier than for the conductive body. This is a reflection that the fundamental cur-  
15     7 rents reside for a longer time in a conductor. For the canonical body, a significant difference between  
16     8 the measured responses and the fundamental fields occur about 0.9 ms for  $b_z$  and about 2 ms for  
17     9  $\frac{\partial b_z}{\partial t}$ . The amplitudes of the IP responses are significantly smaller than those for the conductor. Lastly,  
18     10 there is little IP signal for the resistive body; the IP signal is much smaller than the fundamental re-  
19     11 sponse throughout the given time range. This is a consequence of the small fundamental currents in  
20     12 the resistor.  
21  
22  
23  
2425     13 The decay curves from a sounding location provide insight about the IP response but more is  
26     14 gleaned by looking at data from all sounding locations in the ATEM survey. We focus on  $b_z^{IP}$  for the  
27     15 conductive block at selected time channels. Fig. 5 shows interpolated maps of the observed, funda-  
28     16 mental and IP responses at (a) 0.86 ms and (b) 6.7 ms which are respectively included in the charging  
29     17 and discharging times. For the conductive block, 0.86 ms is close to the peak time when transition  
30     18 from charging to discharging occurs, but it is still included in the charging time. At this time, the ob-  
31     19 servations are dominated by the fundamental response and no negative values, which are the signature  
32     20 of the IP effect, are observed. Subtracting the fundamental however, yields a residual  $d^{IP}$  data map  
33     21 that has a strong negative. This example shows that our EM decoupling procedure can work satisfac-  
34     22 torily. At 6.7 ms, obtaining good IP data are easier because the observed data already show negative  
35     23 values. There is still a weak fundamental field and the subtraction process improves the  $d^{IP}$  response.  
36  
37     24 The  $d^{IP}$  data at 0.86 ms and 6.7 ms shown in Fig. 5 are of sufficient quality to be inverted.  
38  
39  
40  
41  
42  
43  
44  
45  
46  
47  
4849     25 **7.2 Polarization currents**50  
51     26 To evaluate the polarization current shown in eq. (17) for the linear functional, we assumed  $\vec{e}(t) \approx$   
52     27  $\vec{e}^{ref}w^e(t)$  and defined our reference current as  $\vec{j}^{ref} = \sigma_\infty \vec{e}^{ref}$ . That yielded our approximation of  
53     28 the polarization current to be  $\vec{j}^{pol}(t) \approx -\vec{j}^{ref}\tilde{\eta}(t)$ . This approximation says that the polarization  
54     29 current has a fixed direction antiparallel to the reference current and that direction is the same for all  
55     30 times. The only time dependence occurs through the scalar  $\tilde{\eta}(t)$ .  
56  
5758     31 We investigate this by evaluating both reference and polarization currents numerically. From  
59     32 eq. (20), a reference current can be considered as the maximum fundamental current that occurred

1  
2  
3 16 *Seogi Kang and Douglas W. Oldenburg*  
4  
5

6 throughout the time history. To evaluate polarization currents we rearrange eq. (16) as  $\vec{j}^{pol} = \vec{j}^{IP} -$   
7  
8  $\sigma_\infty \vec{e}^{IP}$ . Computation of this subtraction yields the polarization currents.  
9  
10

11 Here we limit our attention to canonical and conductive blocks. Figs 6(a) and (b) show reference  
12 currents for the canonical and conductive blocks, respectively. A transmitter is located at (-200 m, 0  
13 m, 30 m) and marked as a white solid circle in the figure, where  $(\cdot, \cdot, \cdot)$  means a point at (easting,  
14 northing, depth). Reference currents for the canonical block are circular, centered on the transmitter  
15 location, and decay with distance. For the conductive block, additional vortex currents are induced.  
16 We compare these reference currents with the polarization currents. Fig. 7 shows the plan and section  
17 view maps of the polarization currents at 0.86 ms. Comparisons of Figs 6 and 7 clearly show that  
18 polarization currents for both canonical and conductive blocks are oppositely aligned with respect to  
19 their reference current. This was the hypothesized outcome. Fig. 8 shows polarization currents at 6.7  
20 ms, and direction of polarization currents are similar to those at 0.86 ms. This illustrates that direction  
21 of polarization currents after 0.86 ms for both canonical and conductive blocks are almost constant in  
22 time.  
23  
24

25 For an EIP survey conducted over one of the blocks, we expect IP responses that could be ex-  
26 plained by an electric dipole current in a chargeable medium (Seigel 1959). However, for the ISIP  
27 additional complexity arises due to vortex currents induced in a conductor because these generate  
28 complicated polarization currents within the chargeable medium. Our choice of reference currents  
29 effectively incorporates this complicated direction of polarization currents for a conductive medium.  
30  
31

32 20 **7.3 IP currents**  
33  
34

35 21 The IP currents, as provided in eq. (16), are given as  
36  
37

$$38 \quad 43 \quad \vec{j}^{IP} = \sigma_\infty \vec{e}^{IP} + \vec{j}^{pol} \quad (60)$$

40 46 In most analyses, e.g. Smith et al. (1988), the term  $\sigma_\infty \vec{e}^{IP}$  is neglected. We have included this term  
41 47 but with an approximation that  $\vec{e}^{IP} \approx -\nabla\phi$  (eq. 30). Here we can investigate these approximations,  
42 48 and under what circumstances they hold.  
43 49  
50

51 51 Using the forward modelling we can evaluate  $\vec{e}^{IP}$ . This field can be broken into galvanic and in-  
52 52 ductive parts using the Helmholtz decomposition:  $\vec{e} = -\vec{\nabla}\phi - \vec{a}$  so that  $\vec{j}^{IP} = \vec{j}^{pol} - \sigma_\infty \vec{\nabla}\phi^{IP} -$   
53 53  $\sigma_\infty \vec{a}^{IP}$ . In our work we included the effects from the scalar potential but neglected entirely any con-  
54 54 tribution from the vector potential. We look at the contributions of each of these terms for the three  
55 55 cases of canonical, conductive and resistive bodies. Fig. 9 respectively shows plan view maps of  $\vec{j}^{pol}$ ,  
56 56  $-\sigma_\infty \phi^{IP}$ , and  $-\sigma_\infty \vec{a}^{IP}$  for (a) canonical, (b) conductive, and (c) resistive models at 0.86 ms.  
57 57  
58 58

59 59 31 For all three cases the polarization currents have the greatest strength in the body and the strength  
60  
61

1  
2  
3     *On recovering distributed IP information from inductive source time domain electromagnetic data* 17  
45  
6     of these currents is largest in the conductive body and smallest in the resistive body. In all cases,  
7     the polarization currents are the largest contribution to  $\vec{j}^{IP}$ . The second column in Fig. 9 is related  
8     to the scalar potential for the electric field or effectively to the galvanic currents. These exist both  
9     inside and outside the chargeable body. Again, these are largest for the conductive body. We note  
10    that inside the body, these currents have a direction that is opposite to the polarization currents. The  
11    third column is associated with the vector potential for  $\vec{e}^{IP}$  and is associated with vortex currents. The  
12    effects of these currents has not been included in our linearized approximations. These currents are  
13    quite small for the canonical and resistive models. They are most noticeable for the conductive model  
14    where their amplitude starts to be comparable to the galvanic portion. We note that the direction of the  
15    vortex currents inside the body is the same as for the galvanic currents and opposite to the polarization  
16    currents.  
1718     We evaluate  $\vec{j}^{IP}$  and its components at two locations in the body for conductive model. These  
19     are denoted by white stars in the figures. For both points, the polarization currents have the greatest  
20     strength and vortex currents are smaller than the galvanic currents. At both locations the IP current  
21     is smaller than the polarization current because galvanic and vortex IP currents are in the opposite  
22     direction compared to the polarization currents. The results are tabulated in Table 1.  
2324     The above figures provide insight about the three contributions to  $\vec{j}^{IP}$  but of ultimate interest is the  
25     effect of these currents on the measured data. We therefore apply the Biot-Savart law to each current. It  
26     suffices to work with the conductive case. Fig. 10 shows IP responses computed from the polarization  
27     current (stars), galvanic (rectangles) and inductive portions (circles) of the IP current. Here solid and  
28     empty markers show negative and positive signs, respectively. The polarization current has the major  
29     contribution to the IP response although it is larger than the true value. This overshoot is primarily  
30     negated by the galvanic portion of IP responses and further reduced because of the vortex currents.  
31     We notice that the contribution of the galvanic currents is generally larger than those due to the vortex  
32     currents except they are nearly equal near 0.4 ms. At 6.7 ms, the amplitude of the IP response due  
33     to the polarization current is about 130 percent of the true one, while galvanic portion is 30 percent.  
34     These results show that the assumption by Smith et al. (1988) is reasonable, but incorporation of the  
35     galvanic portion to the IP datum is significant and more important at later times. The inductive portion  
36     of the IP responses is small compared to the galvanic portion except for the time before 0.2 ms, and  
37     hence ignoring this inductive portion is generally.  
38  
39  
40  
41  
42  
43  
44  
45  
46  
47  
48  
49  
50  
51  
52  
53  
54  
55  
56  
57  
58  
59  
6031     **7.4    Validations of linearization**32     Forward modelling using eq. (37) requires that we have adequately estimated the IP currents and we  
33     can evaluate their response using the Biot-Savart law. To validate this we first compute approximate

1  
2  
3 18 Seogi Kang and Douglas W. Oldenburg  
4  
5

6 IP currents using eq. (33), and first compare them with the true IP currents. It suffices to work with  
7 the conductive model which is the most challenging. Fig. 11 compares the true and approximate IP  
8 currents at 0.86 ms. The approximate IP currents match well, both in direction and amplitude, with  
9 the true IP currents both inside and outside the body. As shown in Fig. 12 the agreement improves as  
10 time increases.  
11  
12

13 We next test the validity of the computation of IP responses by using the our formulation of  
14 the Biot-Savart law. To do this we compute the “true” IP responses by subtracting the fundamental  
15 response from the observations. We next compute the IP responses by evaluating the Biot-Savart law  
16 with the true IP currents shown in Fig. 12(a). As shown in Fig. 13 the agreement between these  
17 responses is very good after 0.01 ms. This validates the use of the Biot-Savart law (eq. 35). Lastly, we  
18 want to compare responses, evaluated through the Biot Savart law, using our approximated IP currents  
19 (Fig. 12b). The results are shown in Fig. 13. The responses obtained from using our approximate  
20 currents have lower amplitude and differ by 33 percent at the extreme. The difference decreases with  
21 increasing time. Overall the two curves are in reasonable agreement, thus validating our linearized  
22 forward modeling (eq. 37).  
23  
24

25 The same analysis as above was carried out for the canonical and resistive models. As shown  
26 in Fig. 13 the agreement is further improved. We note however, that despite the fact that our linear  
27 functional reasonably explains  $d^{IP}$  data for the resistive case, the IP signals are so small that we likely  
28 cannot distinguish them in practise.  
29  
30

## 31 20 7.5 Effective pseudo-chargeability for ATEM data 32 33

34 In Section 7.5 we showed how to define an effective chargeability when we have multi-transmitters.  
35 For each pixel we have equation:  
36  
37

$$38 \quad 45 \quad 46 \quad 47 \quad \tilde{\eta}_i(t) = \tilde{\eta}_i^I(t) \otimes w_i^e(t), \quad (61)$$

48 where  $\tilde{\eta}_i^I(t)$  is the intrinsic chargeability associated with an individual pixel. The effective time his-  
49 tory of the electric field,  $w_i^e(t)$  is a linear combination of the fundamental electric fields due to the  
50 individual transmitters. We can calculate  $w_i^e(t)$  and carry out the convolution to evaluate the effective  
51 pseudo-chargeability. The IP data can then be forward modelled using eq. (37). We can test eq. (52) by  
52 comparing results with the true IP data obtained via forward modelling. It is only necessary to apply  
53 this to the conductive model.  
54  
55

56 The evaluation of the effective pseudo-chargeability is carried out on a cell by cell basis. For each  
57 cell we first evaluate  $w^e(t)$  (eq. 59). This requires calculating normalized weights shown in eq. (56).  
58 Fig. 14 shows these weights at a single pixel located at (0 m,0 m,-75 m). These decay away from the  
59  
60

1  
2  
3     *On recovering distributed IP information from inductive source time domain electromagnetic data*    19  
4  
51     pixel because of the decay of the sensitivity functions.  $w^e(t)$ , evaluated using eq. (59), is shown in Fig.  
2     15 (solid line) along with  $\hat{w}(t)$  (dashed lines) for each transmitter (the  $w^e(t)$  is dominantly affected by  
3     the  $\hat{w}(t)$  at the center transmitter location (solid circles)).  $w^e(t)$  is convolved with  $\tilde{\eta}^I(t)$  to compute  
4     the effective  $\tilde{\eta}(t)$  for that cell. When this is carried out for each cell then the approximate IP responses  
5     can be computed using eq. (37). These can be compared with the true IP responses. Fig. 16 shows the  
6     comparisons at 0.86 ms. The images are nearly identical in shape but the approximate IP responses are  
7     nearly a factor of two lower than the true values. This is not entirely unexpected. A similar effect was  
8     observed for IP responses for a single transmitter shown in Fig. 13. At 0.86 ms, the approximate value  
9     was about 70 percent of the true  $d^{IP}$ . These results seem to be a worst case scenario. The discrepancy  
10    for a conductive body lessens as time increases and analyses for the canonical and resistive bodies  
11    shows that the approximate and true IP data are in very good agreement.  
12  
13  
14  
15  
16  
17  
18  
19  
20  
21  
22  
23  
24  
25  
26  
27  
28  
29  
30  
31  
32  
33  
34  
35  
36  
37  
38  
39  
40  
41  
42  
43  
44  
45  
46  
47  
48  
49  
50  
51  
52  
53  
54  
55  
56  
57  
58  
59  
6012   **7.6 3D IP inversions**13   Using our linearized sensitivity, we now proceed with 3D IP inversion, which recovers a pseudo-  
14   chargeability given by eq. (37). We limit our attention to the conductive case. For the computation of  
15   the sensitivity we use the true conductivity ( $\sigma_\infty$ ) and then invert data at successive time channels and  
16   recover 3D pseudo-chargeability at multiple times. Our 3D inversion is based upon (Oldenburg & Li  
17   1994; Li & Oldenburg 2000), and it requires some choices for inversion parameters.18   For data uncertainties, we used one percent of the maximum amplitude of the observed data  
19   ( $0.01\max(|\mathbf{d}^{obs}|)$ ). Coefficients for smallness and smoothness are set to  $\alpha_s = 10^{-5}$  and  $\alpha_x = \alpha_y =$   
20    $\alpha_z = 1$ , respectively. The reference model is zero and we also applied a depth weighting. The need  
21   for a depth weighting arises because the sensitivity function  $J$  is primarily controlled by a  $1/r^3$  decay  
22   associated with the Biot-Savart kernels. Thus an ATEM data set is not unlike that commonly acquired  
23   magnetic data where it is well established that a depth weighting is required to image objects at depth.  
24   The following example illustrates this.25   We first generate IP responses at a single time using the linear functional by assuming that the  
26   pseudo-chargeability is unity inside the body and zero outside, as shown in Fig. 17(a). Fig. 17(b)  
27   shows the recovered pseudo-chargeability without depth weighting. The recovered anomalous pseudo-  
28   chargeability is concentrated near the surface and the magnitude of the pseudo-chargeability is under-  
29   estimated; it is  $\sim 0.2$  rather than unity. By using the depth weighting shown in eq. (43), the IP body is  
30   imaged closer to its true depth (Fig. 17b). Also, the magnitude of the recovered pseudo-chargeability  
31   ( $\sim 0.6$ ) is closer to the true value than the result without depth weighting. Based on this analysis, we  
32   use the same depth weighting for our following examples.

1  
2  
3 20 Seogi Kang and Douglas W. Oldenburg  
4  
5

6 1 7.6.1 *Incorrect conductivity*  
7  
8

9 2 The background conductivity  $\sigma_\infty$  plays a central role in our analysis. It is used in the EM decoupling  
10 3 process and it is also needed to compute the linearized sensitivities for inversion. Since we need  
11 4 to estimate  $\sigma_\infty$ , usually through the inversion of EM survey data, it will never be correct. Here we  
12 5 explore some effects of an incorrect conductivity but the consequences are problem dependent.  
13  
14

15 6 We return to our conductive block in a halfspace and evaluate the  $d^{IP}$  data when the background  
16 7 is the true value ( $\sigma_1 = 10^{-3}$  S/m) as well as a factor of two too large ( $2 \times 10^{-3}$  S/m) and a factor of  
17 8 two too small ( $5 \times 10^{-4}$  S/m). The data along a survey line are plotted in Fig. 18.  
18  
19

20 9 We invert these three IP responses, and provide sections of the recovered pseudo-chargeability at  
21 10 0 m-northing. Fig. 19(a), (b) and (c) correspondingly show the recovered pseudo-chargeability when  
22 11 the conductivity is: the true value, too high, or too low. With the correct conductivity the geometry of  
23 12 the IP body is reasonably recovered. When the conductivity is too high, the  $d^{IP}$  have a negative bias  
24 13 that results in larger pseudo-chargeabilities and positive-valued artifacts near the IP body (Fig. 19b).  
25 14 When the conductivity is too small, the IP data have a positive bias and this produces negative-valued  
26 15 artifacts near the IP body (Fig. 19c). However, based on the definition of the pseudo-chargeability  
27 16 shown in eq. (55), the sign of the pseudo-chargeability should be positive. By incorporating positivity  
28 17 as a constraint in the inversion, and re-inverting the IP data having a positive bias, we obtain the result  
29 18 in Fig. 19(d). This is a much better result than Fig. 19(c) and comparison of the observed and predicted  
30 19 data for this case shown in Fig. 20 clearly shows how this constraint prevents the fitting of positive  
31 20 residual fields. We shall use this positivity constraint for our following 3D IP inversion examples.  
32  
33

34 21 The background conductivity is also needed when computing the sensitivity function, since we  
35 22 need the reference electric field, which is dependent on conductivity. An incorrect conductivity will  
36 23 affect the sensitivity function as well. In order to test this, we compute the sensitivity matrix using a  
37 24 half-space conductivity model ( $\sigma_\infty = \sigma_1$ ). Fig. 21 compares the recovered pseudo-chargeability from  
38 25 the 3D IP inversion of the IP datum at 0.86 ms with the true and incorrect sensitivity function using  
39 26 half-space conductivity. There is not a large difference between the two inversions which suggests  
40 27 that an approximate conductivity may still provide sensitivities that are adequate for inversion. This  
41 28 parallels results from EIP where even an approximate conductivity can still yield good results when  
42 29 inverting the data. Thus there is some robustness in our sensitivity function with respect to an incorrect  
43 30 conductivity and even if we not have an accurate 3D conductivity model we can still apply our 3D IP  
44 31 inversion using half-space conductivity so long as the ATEM data includes distinctive IP response  
45 32 such as negative transients.  
46  
47  
48  
49  
50  
51  
52  
53  
54  
55  
56  
57  
58  
59  
60

1  
2  
3     *On recovering distributed IP information from inductive source time domain electromagnetic data* 21  
4  
56     7.6.2 *Extracting intrinsic IP parameters*  
7  
89     2 By applying our inversion to each time channel of  $d^{IP}$  data separately, we can recover 3D dis-  
10    3 tributions of pseudo-chargeability at multiple times. The pseudo-chargeability at each time carries  
11    4 different information about the state of polarization and we can use these to recover information  
12    5 about intrinsic IP parameters. Diverse time-dependent conductivity models such Cole-Cole model  
13    6 and stretched-exponential can be used for this interpretation. We use the Cole-Cole model with  $c = 1$ .  
14    7 We parametrize pseudo-chargeability at a single pixel in terms of chargeability and time constant as  
15    8 described in Section 6.2, and solve a small inverse problem. This parallels (Yuval & Oldenburg 1997;  
16    9 Hördt et al. 2006).21    10 As an example, we use the conductive and chargeable block presented in the previous section  
22    11 and invert 14 time channels of data ranging from 1-10 ms. The EM data are forward modelled using  
23    12 EMTDIP code and the true  $\sigma_\infty$  model is used to evaluate the IP datum and compute the sensitivity  
24    13 function. The recovered pseudo-chargeability from one of the 14 inversions is shown in Fig. 21a. In  
25    14 that pseudo-chargeability model, we select cells that have a pseudo-chargeability value greater than  
26    15 0.001, and then carry out the nonlinear inversion to estimate the time constant ( $\tau$ ) and chargeability ( $\eta$ )  
27    16 for each cell separately. The forward modelling for this inversion is shown in eq. (44), which requires  
28    17  $w^e(t)$ . The  $w^e(t)$  for a pixel in the block is shown in Fig. 15.34    18 Fig. 22(a) and (b) correspondingly show the estimated time constants and chargeability as section  
35    19 maps. The estimated time constants show good agreement with the true value  $\tau = 0.005$ . There is  
36    20 less agreement about chargeability for which the true value is  $\eta = 0.2$ . Recovered values range from  
37    21 about 0.04-0.2 so most values are underestimated. In Fig. 23, we also provide time decays of the  
38    22 observed and predicted pseudo-chargeabilities at a single pixel marked as a black empty rectangle  
39    23 in Fig. 22. The estimated time constant ( $\tau_{est}$ ) and chargeability ( $\eta_{est}$ ) for this pixel are 0.0046 and  
40    24 0.09, respectively. These results imply there is greater stability on recovering the time constant than  
41    25 on recovering chargeability with our approach. Again, similar experiments were carried out for the  
42    26 canonical and resistive bodies and the conclusions were also that the time constant was adequately  
43    27 recovered with better fidelity than was the intrinsic chargeability.51  
52  
53     28 **8 CONCLUSIONS**  
54  
5556     29 In this paper, we have introduced a procedure for recovering IP information from TEM data with  
57    30 inductive sources. Three main steps are required: 1) subtraction of the fundamental responses from  
58    31 the observations to generate IP data, 2) linearization of the IP responses as a function of the pseudo-  
59    32 chargeability, and 3) restoration of 3D pseudo-chargeability at multiple times, and further interpreta-

1  
2  
3 22 Seogi Kang and Douglas W. Oldenburg  
4  
5  
6

7 tion of the pseudo-chargeability to extract intrinsic IP parameters like Cole-Cole model. We used the  
8 ATEM survey to test our IP inversion procedure.

9 The first step requires that we have a good estimate for the background conductivity  $\sigma_\infty$ . This is  
10 important for two reasons. It is first used to generate the fundamental fields that are subtracted from the  
11 observations to produce the IP data. This conductivity is also needed to compute the sensitivities for  
12 our linear relationship between the IP data and pseudo-chargeability. To construct  $\sigma_\infty$  for our work we  
13 used the early time data that was felt to be uncontaminated with significant IP responses and inverted  
14 them with our 3D algorithms. For the mid-time data, subtraction of the fundamental responses from  
15 the observations revealed negative data even though the observations had been positive. At very late  
16 times however, this subtraction process was not necessary since the EM fields had sufficiently decayed.  
17  
18 Maps of the  $d^{IP}$  data can, in themselves, be a useful processing tool for anomaly hunting.

19 The second item, linearization of the IP responses with respect to a pseudo-chargeability, required  
20 that a number of assumptions be made. This pseudo-chargeability is defined as the ratio of the polar-  
21 ization current to a reference current. Unlike the EIP case, the electric fields for an inductive source do  
22 not achieve steady-state and hence neither do the polarization currents. This fundamental difference is  
23 addressed by evaluating the fundamental fields at each location in the earth and generating a reference  
24 electric field that has the direction and magnitude of the field at time when the fundamental field,  
25 which is responsible for charging the earth, reaches its maximum value. The pseudo-chargeability at  
26 a point in the earth thus depends upon the intrinsic chargeability, the reference electric field, and the  
27 time history of the fundamental electric field. The situation becomes more complicated when data  
28 from many transmitters are to be inverted simultaneously because the time history of the electric field  
29 at a point in the earth is different for each transmitter. We handle this by defining an effective pseudo-  
30 chargeability and an associated reference electric field that accommodates, in a least squares fashion,  
31 the effects of all transmitters acting on a single cell.

32 To have confidence in when, and under what circumstances, our approximations are sufficiently  
33 valid, we proceed with a number of rigorous tests. First we introduce 3 test models which are respec-  
34 tively a chargeable block in a halfspace. The block can be conductive, canonical, or resistive with  
35 respect to the background. Our evaluations show that: (a) our choice of reference electric field and its  
36 time history produces a good estimate of the polarization currents; (b) the IP currents are dominated by  
37 the polarization currents, which is an assumption that is often made. However, the galvanic and vortex  
38 currents arising from the scalar and vector potentials in the Helmholtz decomposition of  $e^{IP}$  can be  
39 significant in some circumstances. They both oppose the direction of the polarization currents in the  
40 body. In our work we have included the galvanic currents and neglected the vortex currents which are  
41 almost always smaller than the galvanic currents. (c) Evaluating the IP responses using the Biot-Savart  
42

1  
2  
3 *On recovering distributed IP information from inductive source time domain electromagnetic data* 23  
45  
6 law provides accurate results. (d) With our approximate IP currents, the predicted responses are in rea-  
7  
8 sonably good agreement with those from the true models although they are underestimated for highly  
9 conductive example. These results lead us to infer that our linearized formulation  $d^{IP}(t) = J\tilde{\eta}(t)$  is a  
10  
11 viable representation for the forward modelling at late times when the IP effect is substantial compared  
12  
13 to the EM effects which will occur in the discharging phase. (e) For the multi-transmitter case we de-  
14  
15 rived an effective pseudo-chargeability, which is a linear combination of the pseudo-chargeability of  
16  
17 each transmitter. These were forward modelled with the linearized formulation and compared to the  
18  
19 true responses. The computed responses showed the same shape; the values were underestimated for  
20  
21 the conductive model but were almost identical for the canonical and resistive models.22  
23  
24  
25  
26  
27  
28  
29  
30  
31  
32  
33  
34  
35  
36  
37  
38  
39  
40  
41  
42  
43  
44  
45  
46  
47  
48  
49  
50  
51  
52  
53  
54  
55  
56  
57  
58  
59  
60 The third component is the 3D inversion of the IP data using the linearized formulation to recover  
an effective pseudo-chargeability for each cell. ATEM data have only one receiver for each transmitter  
and a data map at a single time channel is essentially a potential field. The data do not have intrinsic  
resolving power and hence, as in magnetics or gravity inversions, we attempt to counteract this by in-  
troducing a depth weighting. When this is done, our 3D IP inversion recovers a reasonable geometric  
shape and location of the chargeable body but the amplitude is underestimated. An incorrect  $\sigma_\infty$  has  
two effects in the inversion. Firstly it can generates errors in the  $d^{IP}$  data because the fundamental  
field, which is subtracted from the observations, is incorrect. To obtain insight we looked at the ef-  
fects when the  $\sigma_{est}$  was too low or two high. This respectively yielded positive or negative residual  
fields in the IP response. A positivity constraint on the pseudo-chargeability (similar to that used in  
EIP surveys) greatly ameliorated the effects of the positive residuals. The other avenue by which an  
incorrect  $\sigma_\infty$  can affect the inversion is through the sensitivity matrix  $J$ . We showed that even with  
a poor sensitivity function, computed using half-space conductivity model, we recovered important  
information of the chargeable body such as geometric shape and location. Individual inversions are  
carried out at multiple time channels and the pseudo-chargeability as a function of time for each pixel  
is recovered. The pseudo-chargeability for pixels that had significant chargeability were subsequently  
fit to a Cole-Cole model to estimate  $\tau$  and  $\eta$  by assuming  $c = 1$ . The estimated  $\tau$  was close to the true  
value whereas  $\eta$  was underestimated and less robust. This suggests that there is a possibility to extract  
intrinsic IP parameters from the recovered pseudo-chargeability from ATEM surveys.Our IP inversion procedure provides a framework for recovering IP information from inductive  
source EM surveys and in particular from ATEM surveys that are commonly flown. Our examples  
show: (a) that the horizontal location of a target body can be well recovered; (b) the overall geometry  
might be recovered but much of that inference requires a depth weighting to be included; (c) we can  
recover estimates of intrinsic  $\tau$  and  $\eta$  that may be useful for distinguishing between two chargeable  
targets. Our procedure depends on having a good estimate for the background conductivity and this

24     *Seogi Kang and Douglas W. Oldenburg*

1 aspect this should be carefully investigated in future practical applications of our inversion methodol-  
2 ogy. Other areas for follow-up research include quantitative depth resolution of the airborne IP surveys  
3 and inversions, and robust inversion strategy to extract intrinsic IP parameters from TEM data. Lastly,  
4 our numerical examples only treated the ATEM survey, but the procedure is applicable to other types  
5 of inductive source TEM survey such as large-loop TEM with many receivers. There will be details  
6 that need to be addressed for those applications but the work presented here provides the fundamen-  
7 tal backgrounds for those future studies whose goal is to extract some information about polarization  
8 from an inductive time domain system.

9     **ACKNOWLEDGMENTS**

10 We wish to thank David Marchant for providing EMTDIP code, and other UBC-GIF members for  
11 their constructive comments. We would like to thank Rowan Cockett and Lindsey Heagy for their  
12 contributions to SimPEG (<http://www.simpeg.xyz>).

13     **REFERENCES**

- 14 Chen, J. & W. Oldenburg, D., 2003. 3-D inversion of magnetic induced polarization data, *ASEG Extended*  
15 *Abstracts*, 1(1), 1–11.
- 16 Cockett, R., Kang, S., Heagy, L. J., Pidlisecky, A., & Oldenburg, D. W., 2015. SimPEG: An open source  
17 framework for simulation and gradient based parameter estimation in geophysical applications (submitted),  
18 *Computers and geoscience*.
- 19 Cole, K. S. & Cole, R. H., 1941. Dispersion and absorption in dielectrics i. alternating current characteristics,  
20 *The Journal of Chemical Physics*, 9(4).
- 21 ElKaliouby, H. & Eldiwany, E., 2004. Transient electromagnetic responses of 3D polarizable body, *Geo-*  
22 *physics*, 69(2), 426–430.
- 23 Fiandaca, G., Auken, E., Christiansen, A. V., & Gazoty, A., 2012. Time-domain-induced polarization: Full-  
24 decay forward modeling and 1D laterally constrained inversion of Cole-Cole parameters, *Geophysics*, 77(3),  
25 E213.
- 26 Fink, J., McAlister, E., Sternberg, B., Wieduwilt, W., & Ward, S., 1990. *Induced Polarization Applications*  
27 *and Case Histories*, Society of Exploration Geophysicists.
- 28 Flis, M. F., Newman, G. A., & Hohmann, G. W., 1989. Induced polarization effects in time domain electromag-  
29 netic measurements, *Geophysics*, 54(4), 514–523.
- 30 Haber, E., 2014. *Computational Methods in Geophysical Electromagnetics*, Society for Industrial and Applied  
31 Mathematics, Philadelphia, PA.
- 32 Hodges, G. & Chen, T., 2014. IP effect in airborne TDEM data: Model studies and field examples, *SEG*  
33 *Technical Program Expanded Abstracts*, 158, 828–832.

4  
3      *On recovering distributed IP information from inductive source time domain electromagnetic data*    25  
5

- 6      Hördt, A., Hanstein, T., Höning, M., & Neubauer, F. M., 2006. Efficient spectral IP-modelling in the time  
7      domain, *Journal of Applied Geophysics*, **59**(2), 152–161.
- 8      Kang, S. & W. Oldenburg, D., 2015. Recovering IP information in airborne-time domain electromagnetic data,  
9      *ASEG Extended Abstracts*, **1**(1), 1–4.
- 10     Kang, S., Noh, K., Seol, S. J., & Byun, J., 2014. mCSEM inversion for CO<sub>2</sub> sequestration monitoring at a  
11     deep brine aquifer in a shallow sea.
- 12     Kang, S., W. Oldenburg, D., & S. McMillan, M., 2015. 3D IP Inversion of Airborne EM data at Tli Kwi Cho,  
13     *ASEG Extended Abstracts*, **1**(1), 1–4.
- 14     Kelley, C. T., 1999. *Iterative Methods for Optimization*, Society for Industrial and Applied Mathematics.
- 15     Kemna, A., Binley, A., Cassiani, G., Niederleithinger, E., Revil, A., Slater, L., Williams, K. H., Orozco, A. F.,  
16     Haegel, F. H., Hördt, A., Kruschwitz, S., Leroux, V., Titov, K., & Zimmermann, E., 2012. An overview  
17     of the spectral induced polarization method for near-surface applications, *Near Surface Geophysics*, **10**(6),  
18     453–468.
- 19     Kohlrausch, R., 1854. Theorie des elektrischen Rückstandes in der Leidener Flasche, *Annalen der Physik*,  
20     **167**(2), 179–214.
- 21     Kratzer, T. & Macnae, J., 2012. Induced polarization in airborne EM, *Geophysics*, **77**(5), E317–E327.
- 22     Kwan, K., Prikhodko, A., Legault, J. M., Plastow, G., Xie, J., & Fisk, K., 2015. Airborne Inductive Induced  
23     Polarization Chargeability Mapping of VTEM Data, pp. 1–5.
- 24     Li, Y. & Oldenburg, D. W., 1996. 3-d inversion of magnetic data, *Geophysics*, **61**(2), 394–408.
- 25     Li, Y. & Oldenburg, D. W., 2000. 3-D inversion of induced polarization data, *Geophysics*, **65**(6), 1931–1945.
- 26     Marchant, D., Haber, E., & Oldenburg, D. W., 2012. Inductive source induced polarization, *Geophysical  
27     Journal International*, **192**(2), 602–612.
- 28     Marchant, D., Haber, E., & Oldenburg, D., 2013. Recovery of 3d ip distribution from airborne time-domain  
29     em, *ASEG Extended Abstracts*, **144**, 1–4.
- 30     Marchant, D., Haber, E., & Oldenburg, D. W., 2014. Three-dimensional modeling of ip effects in time-domain  
31     electromagnetic data, *Geophysics*, **79**(6), E303–E314.
- 32     Oldenburg, D. & Li, Y., 1994. Inversion of induced polarization data, *Geophysics*, **59**(9), 1327–1341.
- 33     Oldenburg, D. W. & Li, Y., 2005. *5. Inversion for Applied Geophysics: A Tutorial*, chap. 5, pp. 89–150.
- 34     Pelton, W., Ward, S., Hallof, P., Sill, W., & Nelson, P., 1978. MINERAL DISCRIMINATION AND RE-  
35     MOVAL OF INDUCTIVE COUPLING WITH MULTIFREQUENCY IP, *Geophysics*, **43**(3), 588–609.
- 36     Routh, P. S. & Oldenburg, D. W., 2001. Electromagnetic coupling in frequency-domain induced polarization  
37     data: a method for removal, *Geophysical Journal International*, **145**(1), 59–76.
- 38     Seigel, H., 1959. Mathematical formulation and type curves for induced polarization, *Geophysics*, **24**(3),  
39     547–565.
- 40     Seigel, H., 1974. The magnetic induced polarization (mip) method, *Geophysics*, **39**(3), 321–339.
- 41     Smith, R. S. & Klein, J., 1996. A special circumstance of airborne inducedpolarization measurements, *Geo-  
42     physics*, **61**(1), 66–73.

1  
2  
3 26 *Seogi Kang and Douglas W. Oldenburg*  
4  
5  
6  
7  
8  
9  
10  
11  
12  
13  
14  
15  
16  
17  
18  
19  
20  
21  
22  
23  
24  
25  
26  
27  
28  
29  
30  
31  
32  
33  
34  
35  
36  
37  
38  
39  
40  
41  
42  
43  
44  
45  
46  
47  
48  
49  
50  
51  
52  
53  
54  
55  
56  
57  
58  
59  
60

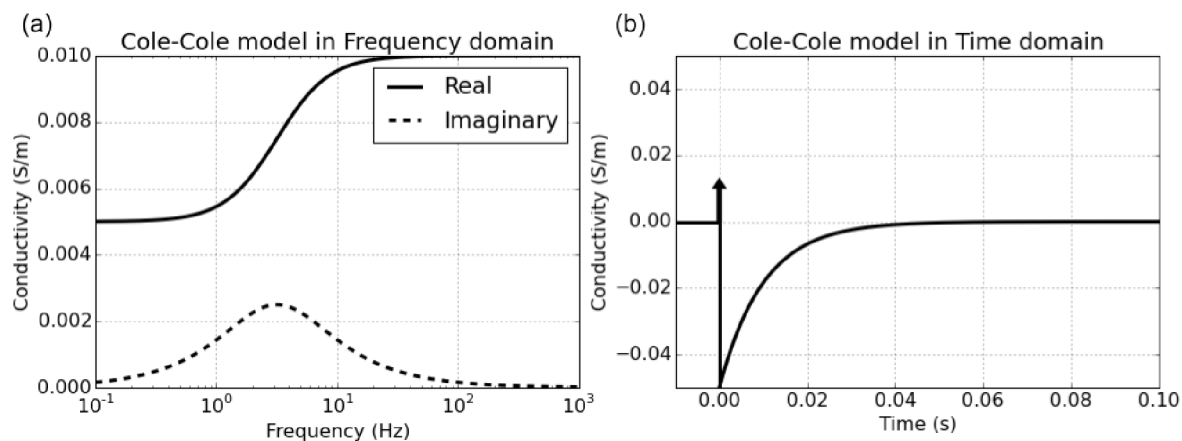
- 1 Smith, R. S., Walker, P., Polzer, B., & West, G. F., 1988. The time-domain electromagnetic response of  
2 polarizable bodies: an approximate convolution algorithm, *Geophysical Prospecting*, **36**(April), 772–785.
- 3 Weidelt, P., 1982. Response characteristics of coincident loop transient electromagnetic systems, **47**(September), 1325–1330.
- 5 Xu, Z. & Zhdanov, M., 2015. Three-dimensional cole-cole model inversion of induced polarization data based  
6 on regularized conjugate gradient method, *Geoscience and Remote Sensing Letters, IEEE*, **12**(6), 1180–1184.
- 7 Yee, K., 1966. Numerical solution of initial boundary value problems involving maxwell's equations in  
8 isotropic media, *Antennas and Propagation, IEEE Transactions on*, **14**(3), 302–307.
- 9 Yuval & Oldenburg, D., 1997. Computation of colecole parameters from ip data, *Geophysics*, **62**(2), 436–448.

1  
2  
3      *On recovering distributed IP information from inductive source time domain electromagnetic data*    27  
4  
5  
6

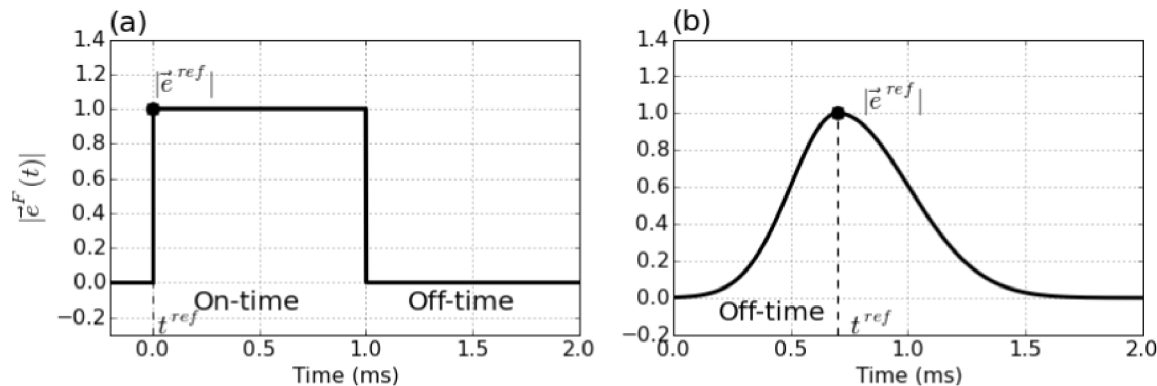
7      **Table 1.** Amplitudes of decomposed IP currents at two marked points (white stars) shown in Fig. 10(b). Units  
8      in  $A/m^2$

Division	$ \vec{j}^{IP} $	$ \vec{j}^{pol} $	$ \sigma_\infty \vec{\nabla} \phi^{IP} $	$ \sigma_\infty \vec{d}^{IP} $
Left	$1.5 \times 10^{-10}$	$2.5 \times 10^{-10}$	$7.6 \times 10^{-11}$	$1.9 \times 10^{-12}$
Right	$5.4 \times 10^{-11}$	$1.2 \times 10^{-10}$	$3.5 \times 10^{-11}$	$3.3 \times 10^{-11}$

1  
2  
3 28 Seogi Kang and Douglas W. Oldenburg  
4  
5



21  
22 **Figure 1.** Cole-Cole model in frequency domain (a) and time (b) domain. The Cole-Cole parameters are  $\sigma_\infty =$   
23  
24  $10^{-2}$  S/m,  $\eta = 0.5$ ,  $\tau = 0.01$ , and  $c=1$ .



39  
40 **Figure 2.** Conceptual diagram for the amplitude of the fundamental electric fields. (a) EIP and (b) ISIP cases.  
41  
42  
43  
44  
45  
46  
47  
48  
49  
50  
51  
52  
53  
54  
55  
56  
57  
58  
59  
60

1  
2  
3  
4 *On recovering distributed IP information from inductive source time domain electromagnetic data* 29  
5  
6  
7  
8  
9  
10  
11  
12  
13  
14  
15  
16  
17  
18  
19  
20  
21  
22  
23  
24  
25  
26  
27  
28  
29  
30  
31  
32  
33  
34  
35  
36  
37  
38  
39  
40  
41  
42  
43  
44  
45  
46  
47  
48  
49  
50  
51  
52  
53  
54  
55  
56  
57  
58  
59  
60

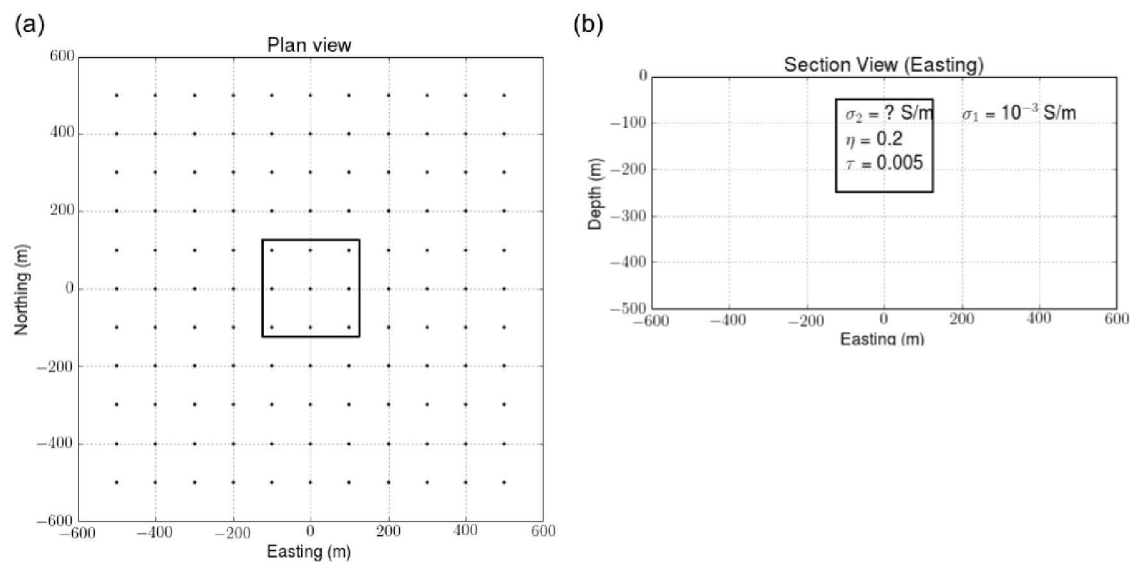
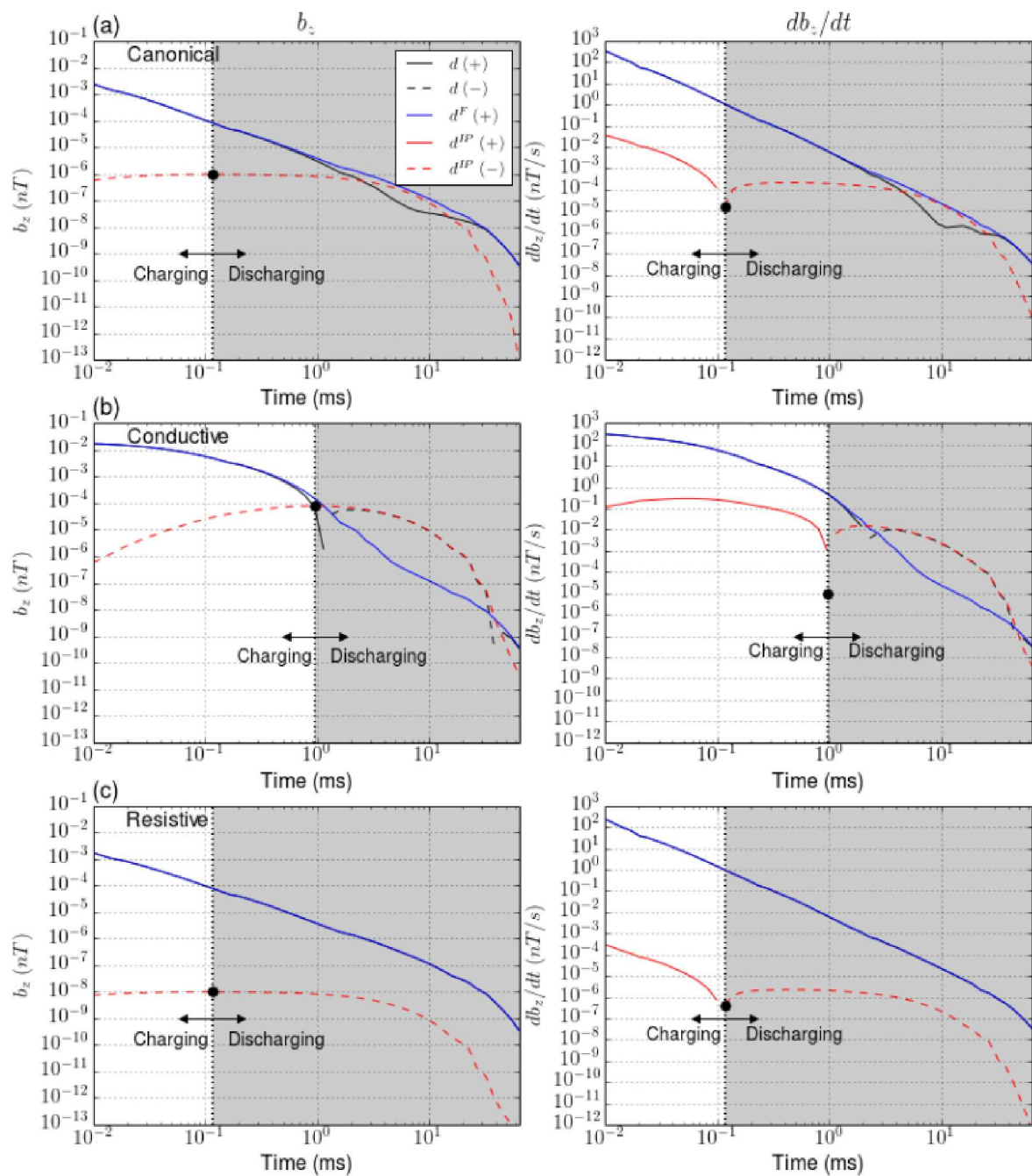


**Figure 3.** Plan (a) and section b) views of the IP model. The solid line in (a) delineates the boundary of the IP body. Solid circles in (a) denote the sounding locations. In (b) the conductivity  $\sigma_2$  is variable so that canonical, conductive and resistive blocks can be examined

30 Seogi Kang and Douglas W. Oldenburg



50 **Figure 4.** Time decaying curves of the observations ( $d$ ; black line), fundamental ( $d^F$ ; blue line) and IP ( $d^{IP}$ ; red line) responses. All three cases: (a) canonical, (b) conductive and (c) resistive are presented. Right and left  
 51 panels show  $b_z$  and  $\frac{\partial b_z}{\partial t}$ . Black dotted line indicates the maximum polarization time.  
 52  
 53  
 54

## On recovering distributed IP information from inductive source time domain electromagnetic data 31

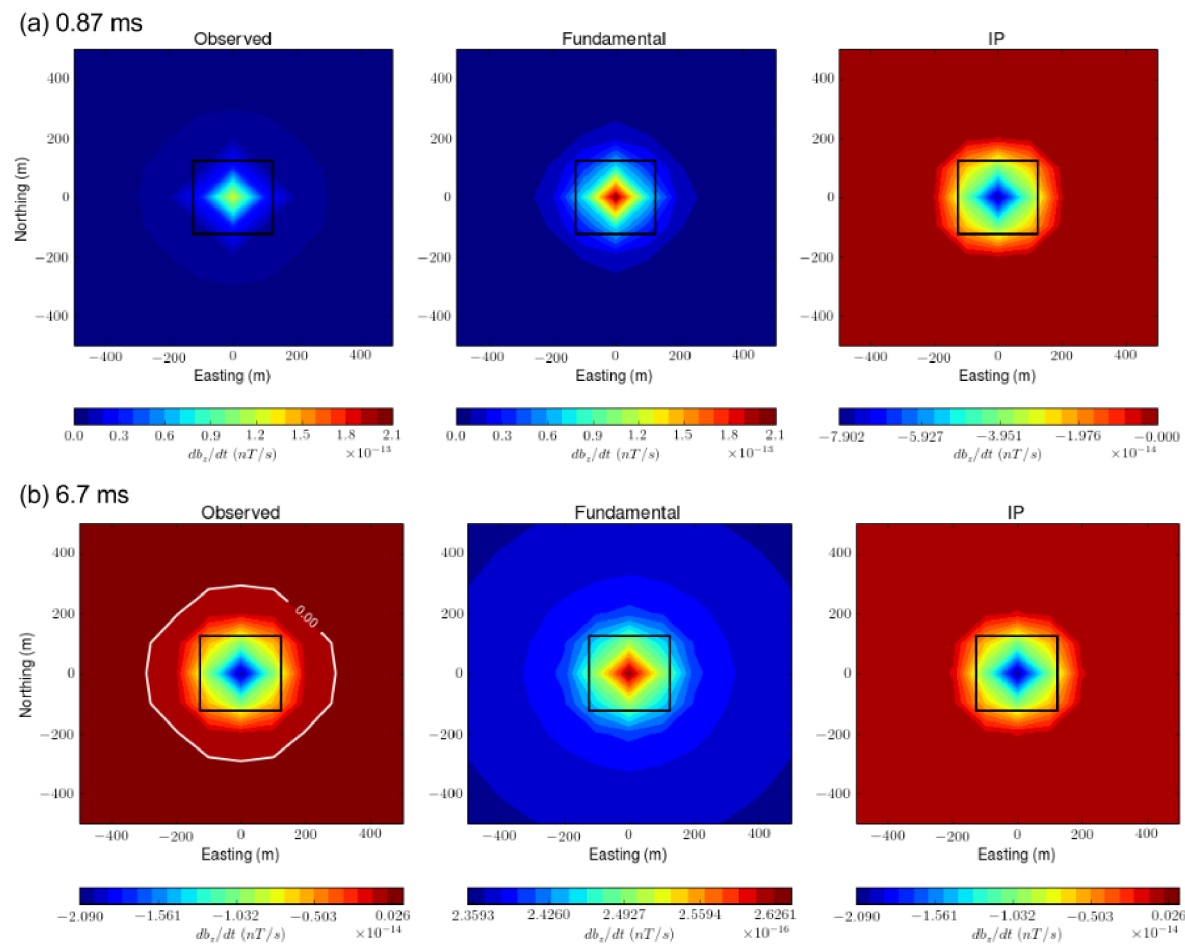


**Figure 5.** Interpolated maps of observed (left panel), fundamental (middle panel) and IP (right panel) responses. Two time channels at (a) 0.86 ms and (b) 6.7 ms are presented. White line contours a zero-crossing in the observed response.

32 Seogi Kang and Douglas W. Oldenburg

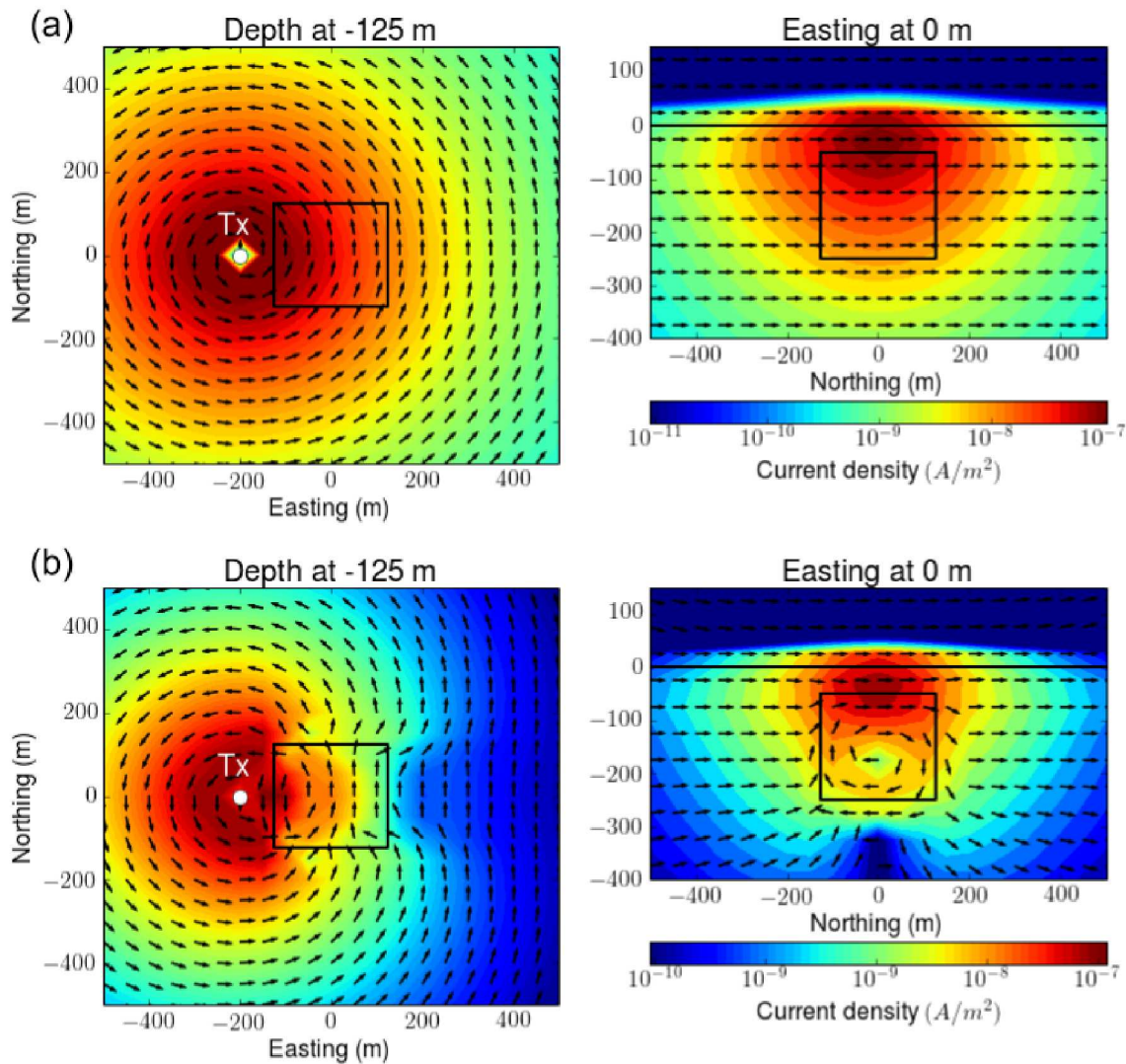


**Figure 6.** Maps of reference currents: (a) canonical and (b) conductive models. Left and right panel show plan and section views at -125 m-depth and 0 m-easting, respectively. A transmitter is located at (-200 m, 0 m, 30 m). Black arrows and colored background indicate the direction and amplitude of the current, respectively. The black solid line outlines the boundary of chargeable body.

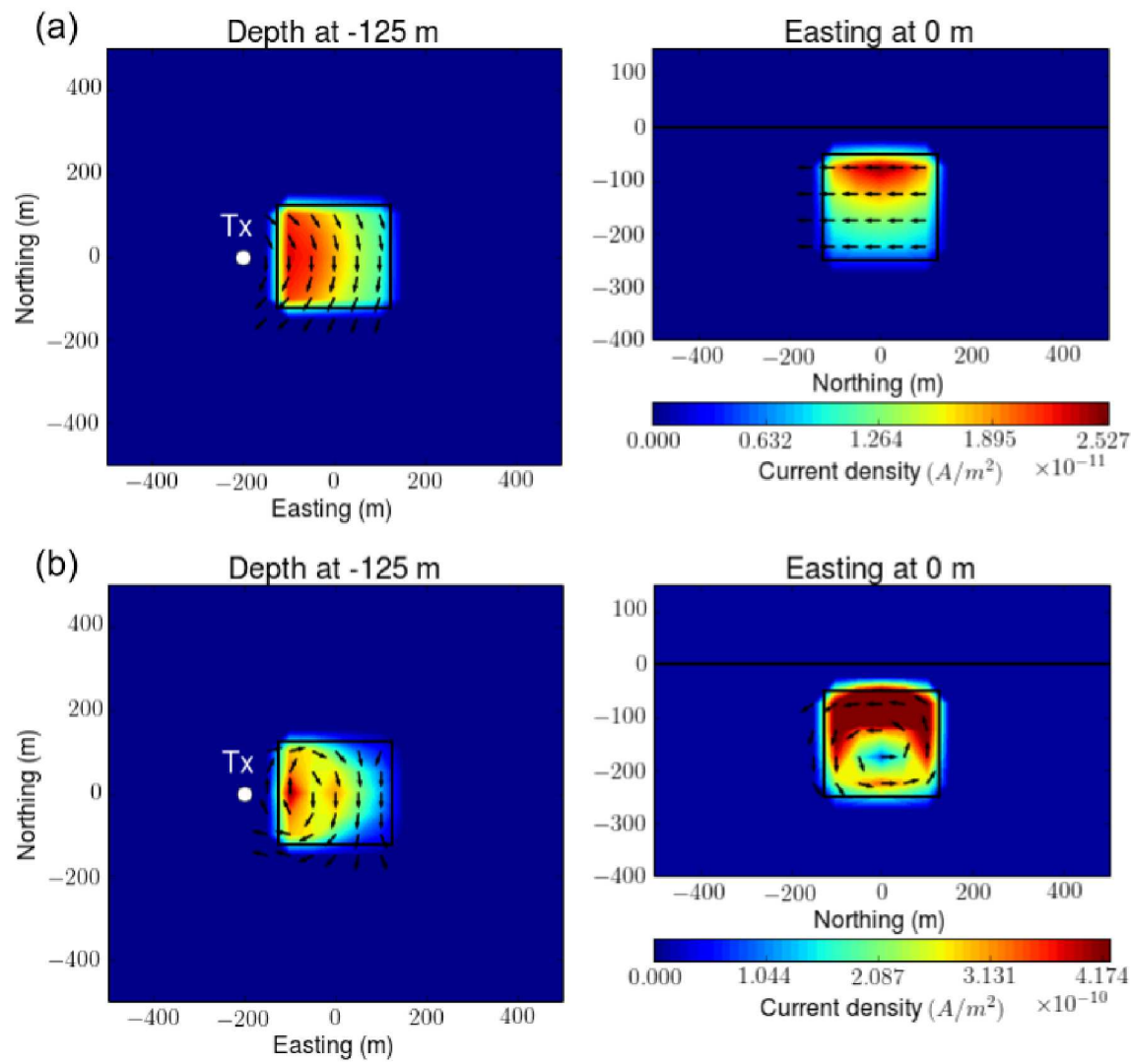


**Figure 7.** Maps of polarization currents: (a) canonical and (b) conductive models at 0.86 ms. Left and right panels show plan and section views at -125 m-depth and 0 m-easting, respectively. A transmitter is located at (-200 m, 0 m, 30 m). Black arrows and shaded values indicate the direction and amplitude of the current, respectively. Black solid outlines boundary of the surface or the chargeable body.

1  
2  
3  
4 34 Seogi Kang and Douglas W. Oldenburg  
5  
6  
7  
8  
9  
10  
11  
12  
13  
14  
15  
16  
17  
18  
19  
20  
21  
22  
23  
24  
25  
26  
27  
28  
29  
30  
31  
32  
33  
34  
35  
36  
37  
38  
39  
40  
41  
42  
43  
44  
45  
46  
47  
48  
49  
50  
51  
52  
53  
54  
55  
56  
57  
58  
59  
60

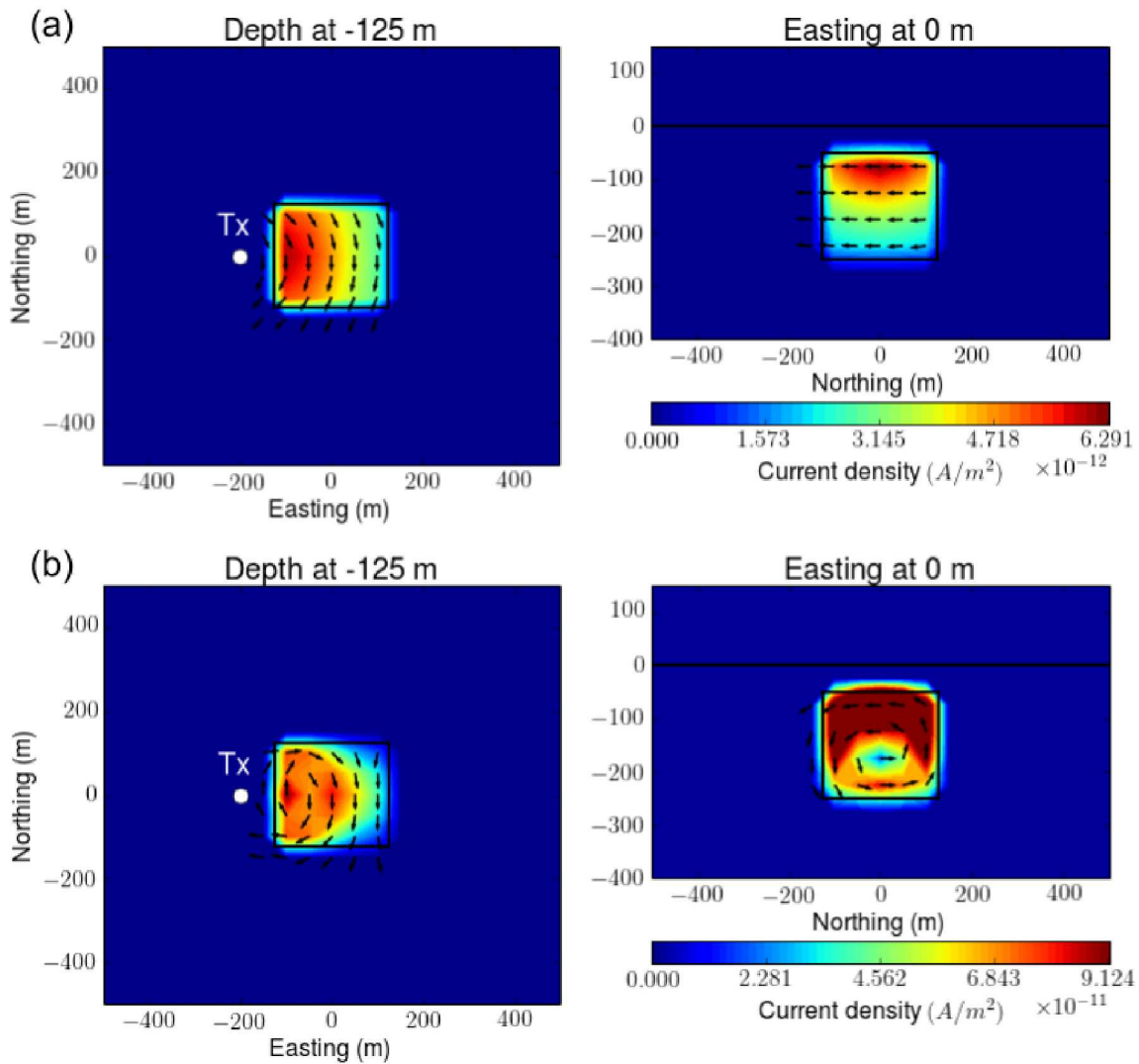


**Figure 8.** Maps of polarization currents: (a) canonical and (b) conductive models at 6.7 ms. Left and right panels show plan and section views at -125 m-depth and 0 m-easting, respectively. A transmitter is located at (-200 m, 0 m, 30 m). Black arrows and shaded values indicate the direction and amplitude of the current, respectively. Black solid outlines boundary of the surface or the chargeable body.

## On recovering distributed IP information from inductive source time domain electromagnetic data 35

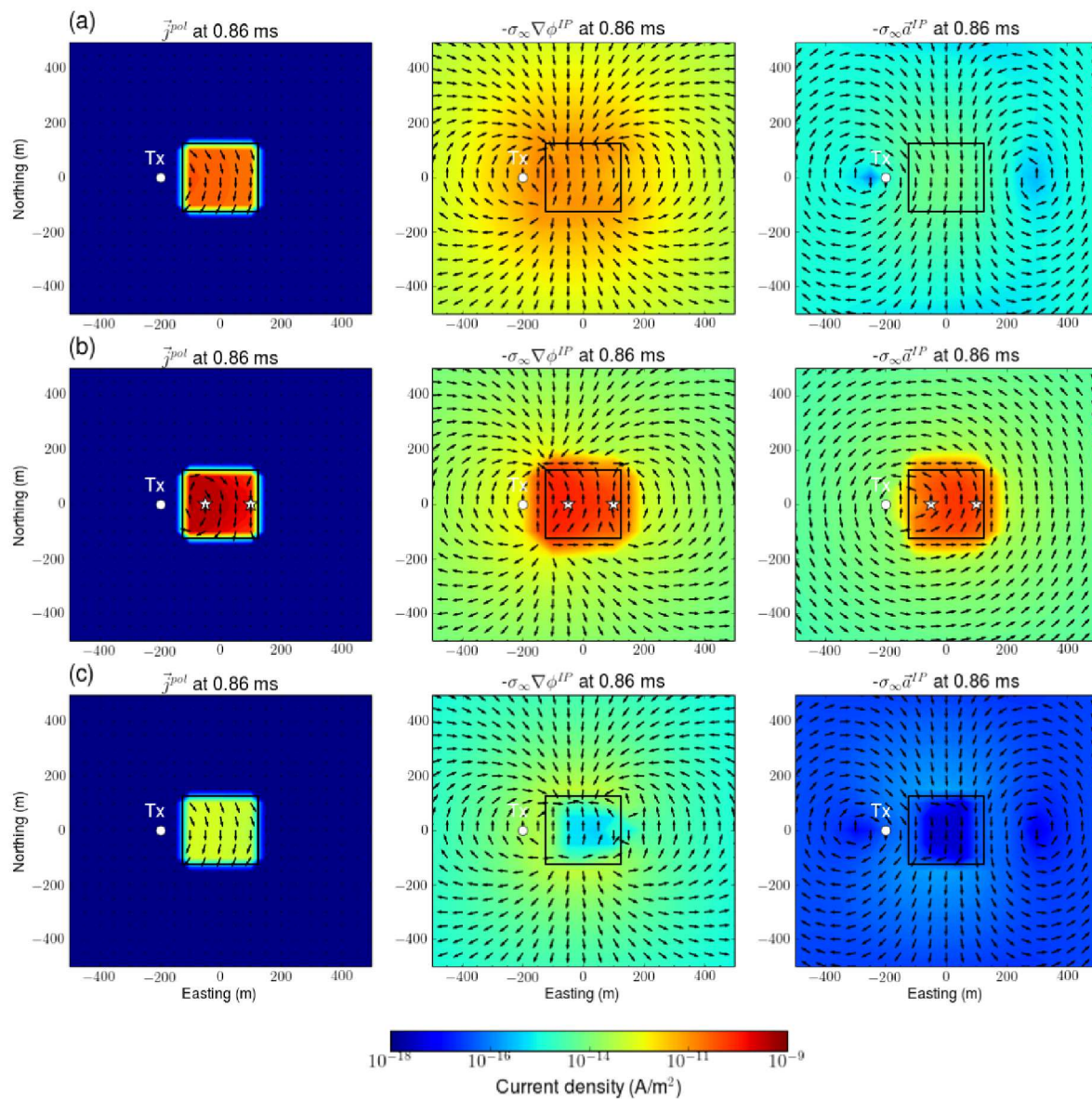


**Figure 9.** Decomposition of the IP currents as  $\vec{j}^{pol}$  (left panel),  $-\sigma_\infty \vec{\nabla} \phi^{IP}$  (middle panel), and  $-\sigma_\infty \vec{a}^{IP}$  (right panel) at 0.86 ms. Plan view maps of the currents at -125 m-depth are shown. (a) Canonical, (b) conductive, and (c) resistive cases.

36 Seogi Kang and Douglas W. Oldenburg

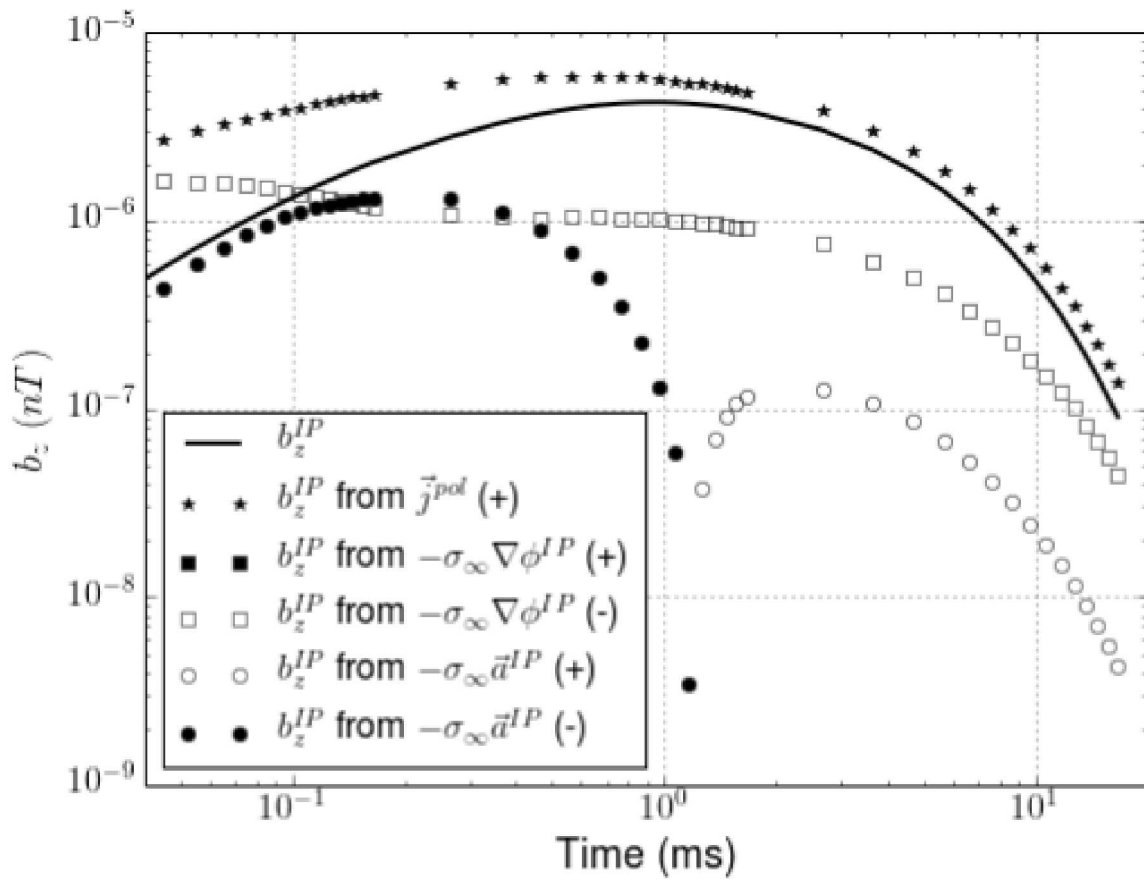


**Figure 10.** Comparisons of contributions of  $\vec{j}^{pol}$ ,  $-\sigma_\infty \vec{\nabla} \phi^{IP}$ , and  $-\sigma_\infty \vec{a}^{IP}$  to the observed IP responses. Solid line indicates true  $b_z^{IP}$  responses. Stars, rectangles, and circles correspondingly indicate each IP response generated by applying Biot-Savart law to  $\vec{j}^{pol}$ ,  $-\sigma_\infty \vec{\nabla} \phi^{IP}$ , and  $-\sigma_\infty \vec{a}^{IP}$ . Empty and solid markers represent positive and negative values, respectively.

1  
2  
3  
4  
5  
6  
7  
8  
9  
10  
11  
12  
13  
14  
15  
16  
17  
18  
19  
20  
21  
22  
23  
24  
25  
26  
27  
28  
29  
30  
31  
32  
33  
34  
35  
36  
37  
38  
39  
40  
41  
42  
43  
44  
45  
46  
47  
48  
49  
50  
51  
52  
53  
54  
55  
56  
57  
58  
59  
60

On recovering distributed IP information from inductive source time domain electromagnetic data 37

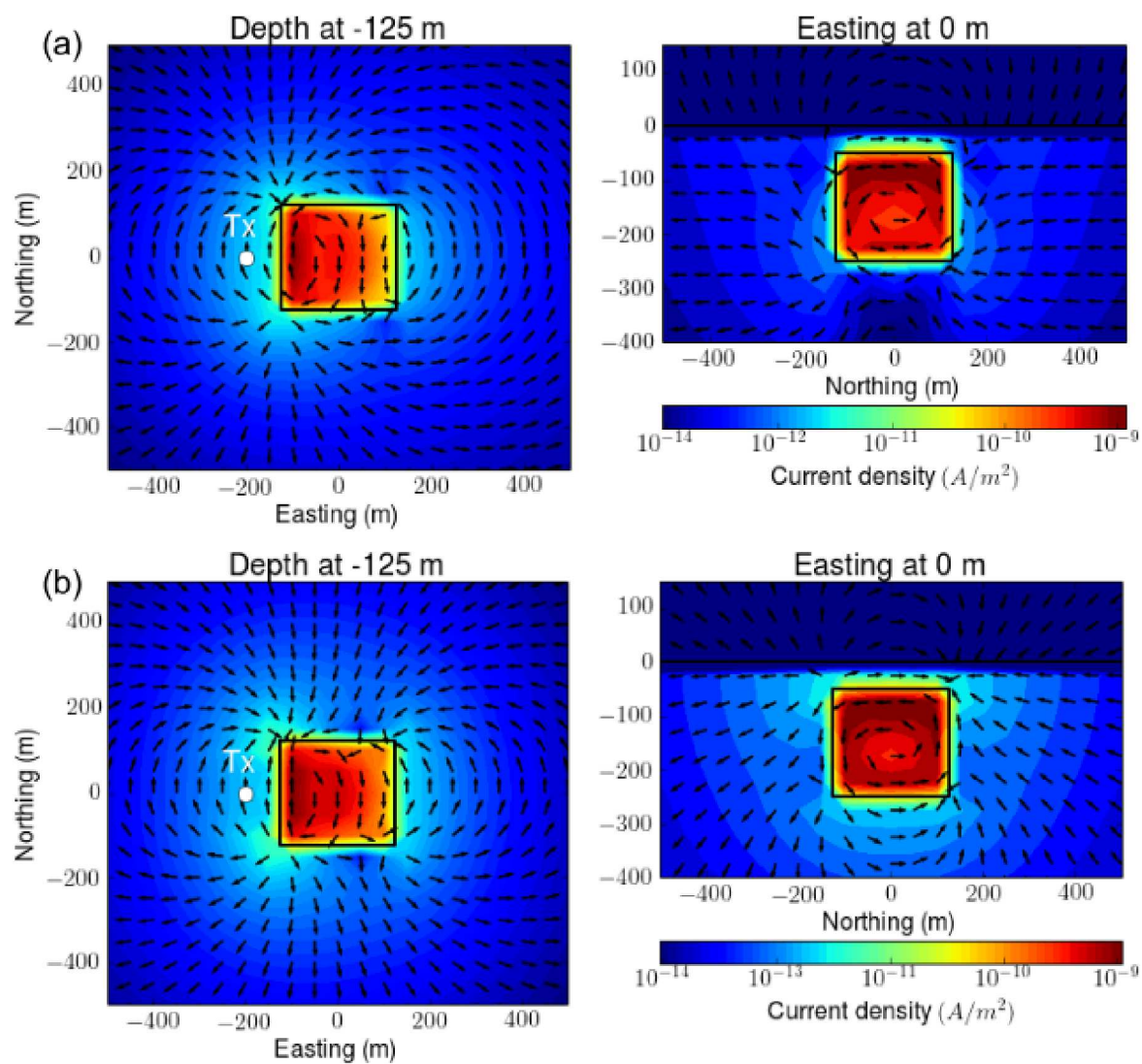


Figure 11. Interpolated maps of (a) true and (b) approximate IP currents at 0.86 ms. Left and right columns show plan and section view maps at -125 m-depth and 0 m-easting, respectively.

38 Seogi Kang and Douglas W. Oldenburg

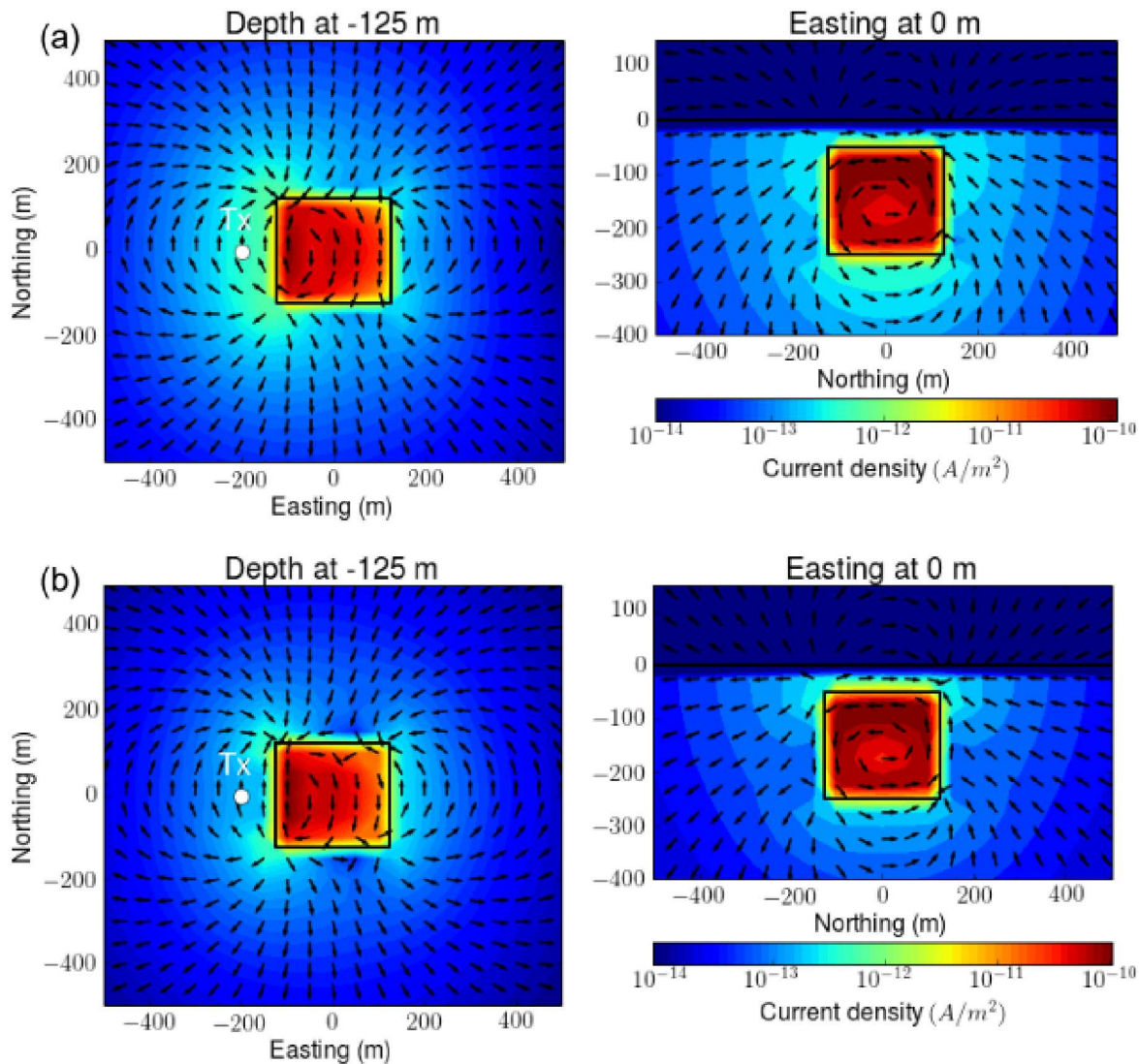
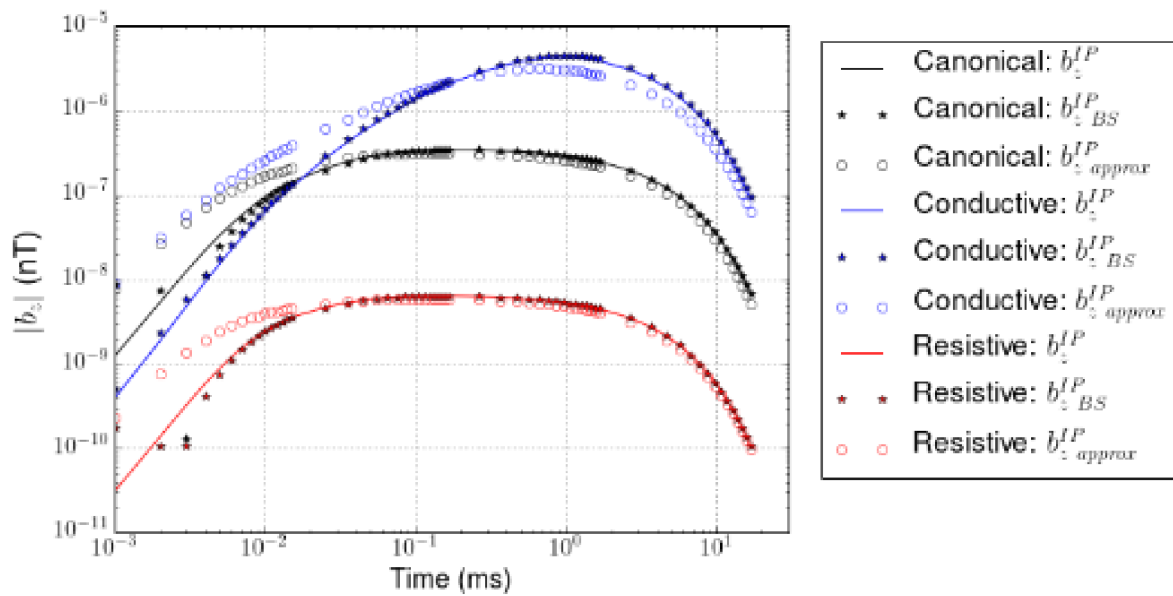


Figure 12. Interpolated maps of (a) true and (b) approximate IP currents at 6.7 ms. Left and right columns show plan and section view maps at -125 m-depth and 0 m-easting, respectively.

## On recovering distributed IP information from inductive source time domain electromagnetic data 39



**Figure 13.** Comparison of true and approximate IP responses ( $b_z^{IP}$ ). Black, blue, and red color respectively indicate canonical, conductive, and resistive cases. Solid lines indicate true  $b_z^{IP}$  computed by subtraction process. The stars are the application of Biot-Savart to true IP current and generate  $b_z^{IP,BS}$ . Empty circles show our approximate  $b_z^{IP,approx}$  response.

40 *Seogi Kang and Douglas W. Oldenburg*

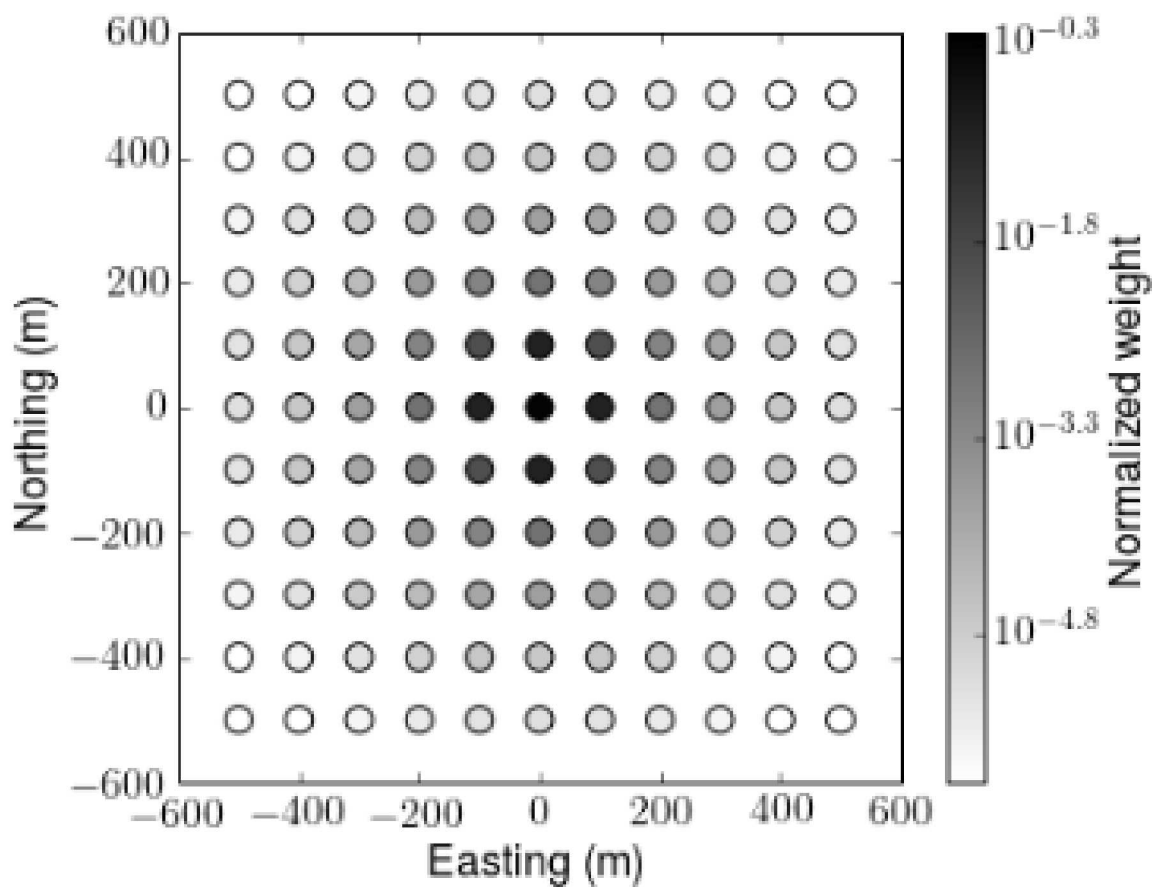


**Figure 14.** Normalized weights for the conductive case for all transmitter locations. A single pixel located at (0 m, 0 m, -75 m) is used.

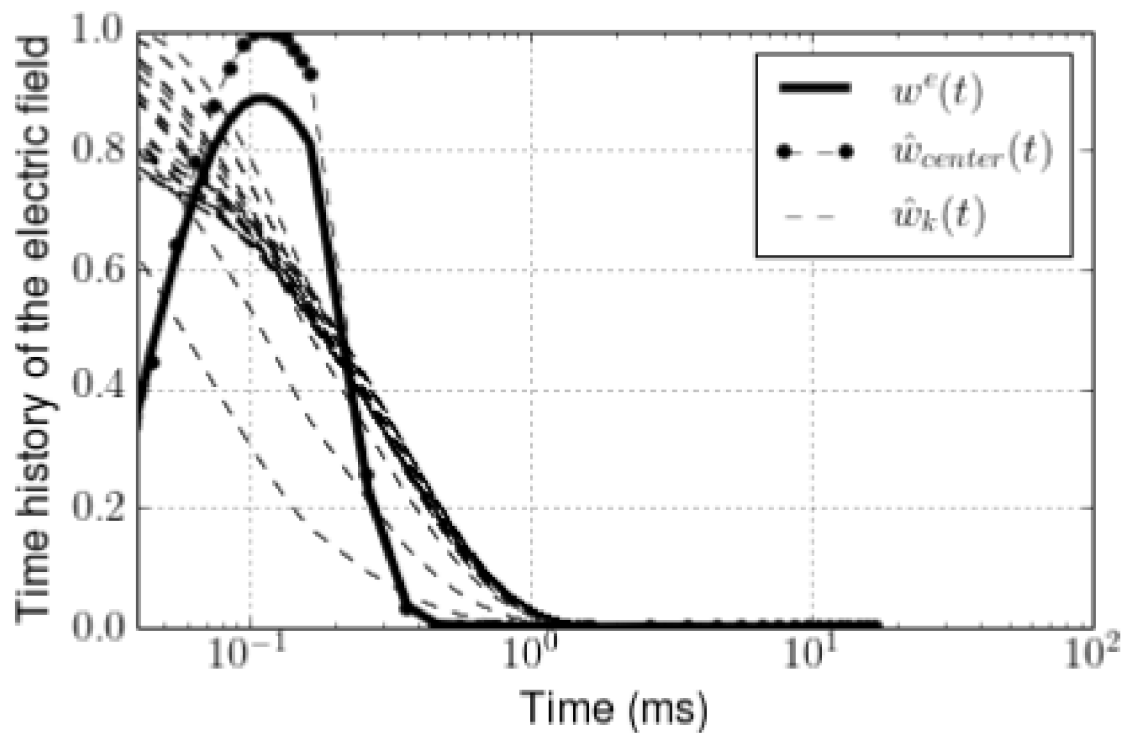


**Figure 15.** Time decays of  $w^e(t)$  and  $\hat{w}(t)$  for the conductive case. A single pixel located at (0 m, 0 m, -75 m) is used. Solid line and dashed lines correspond to  $w^e(t)$  and  $\hat{w}_k(t)$  for all transmitters ( $k = 1, \dots, nTx$ );  $\hat{w}_k$  at the center transmitter located at (0 m, 0 m, 30 m) is marked as solid circles.

42 Seogi Kang and Douglas W. Oldenburg

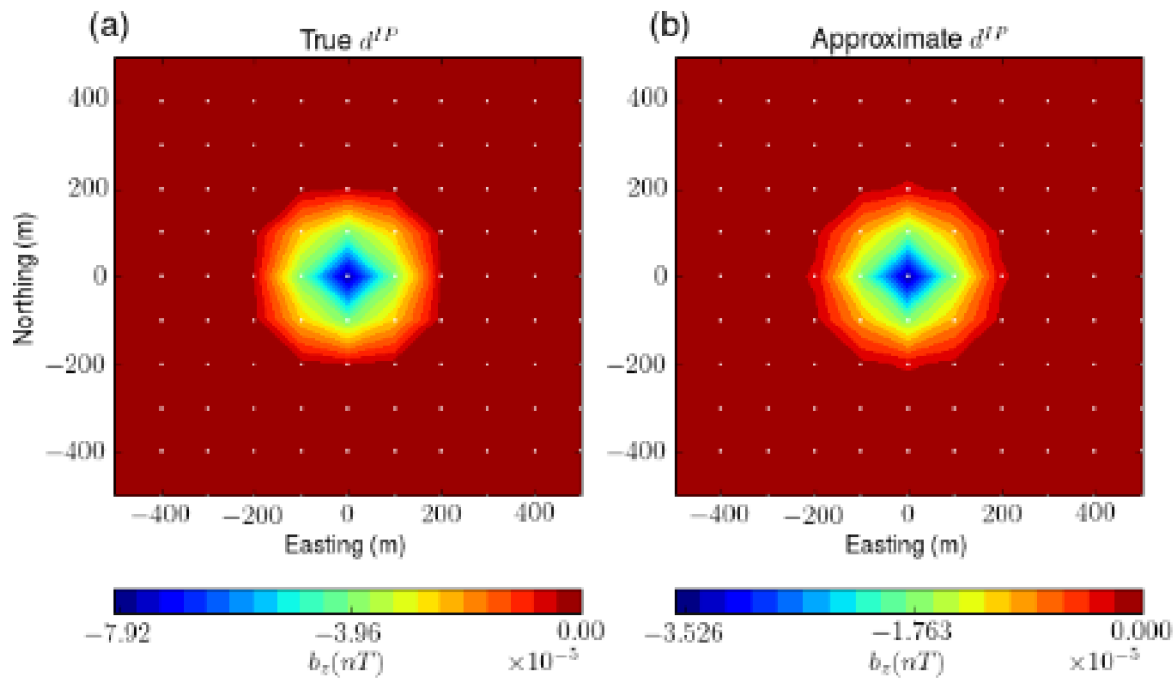


Figure 16. Comparison of true and approximate  $b_z^{IP}$  responses at 0.86 ms on plan view map.

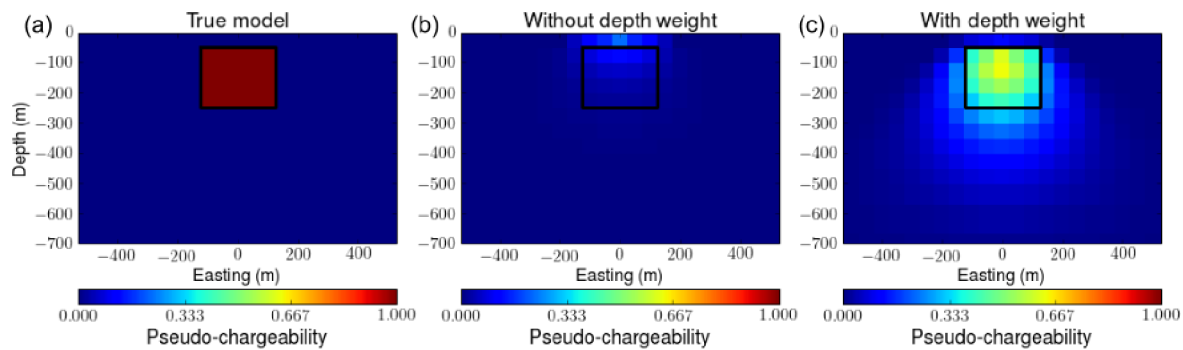
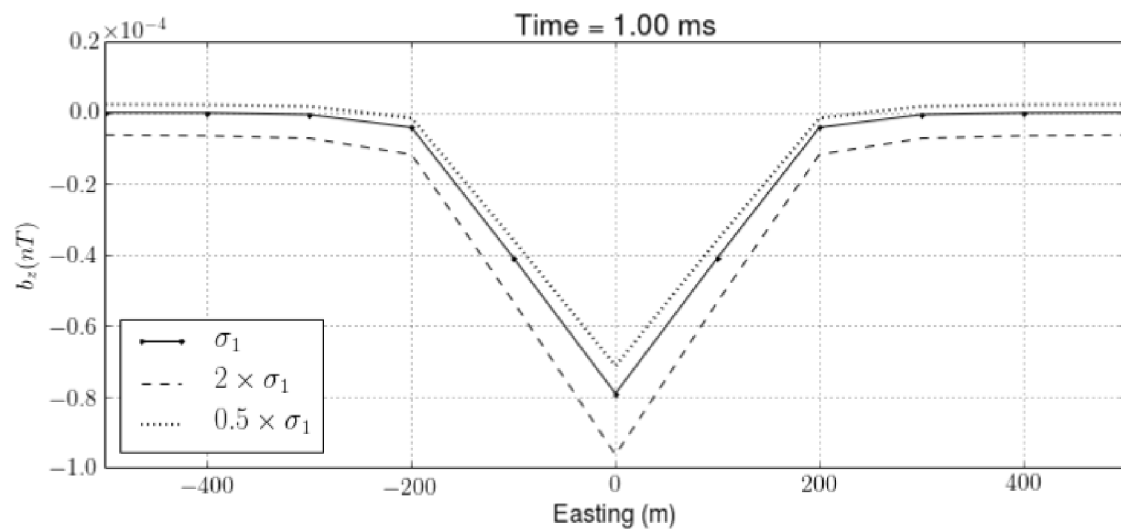
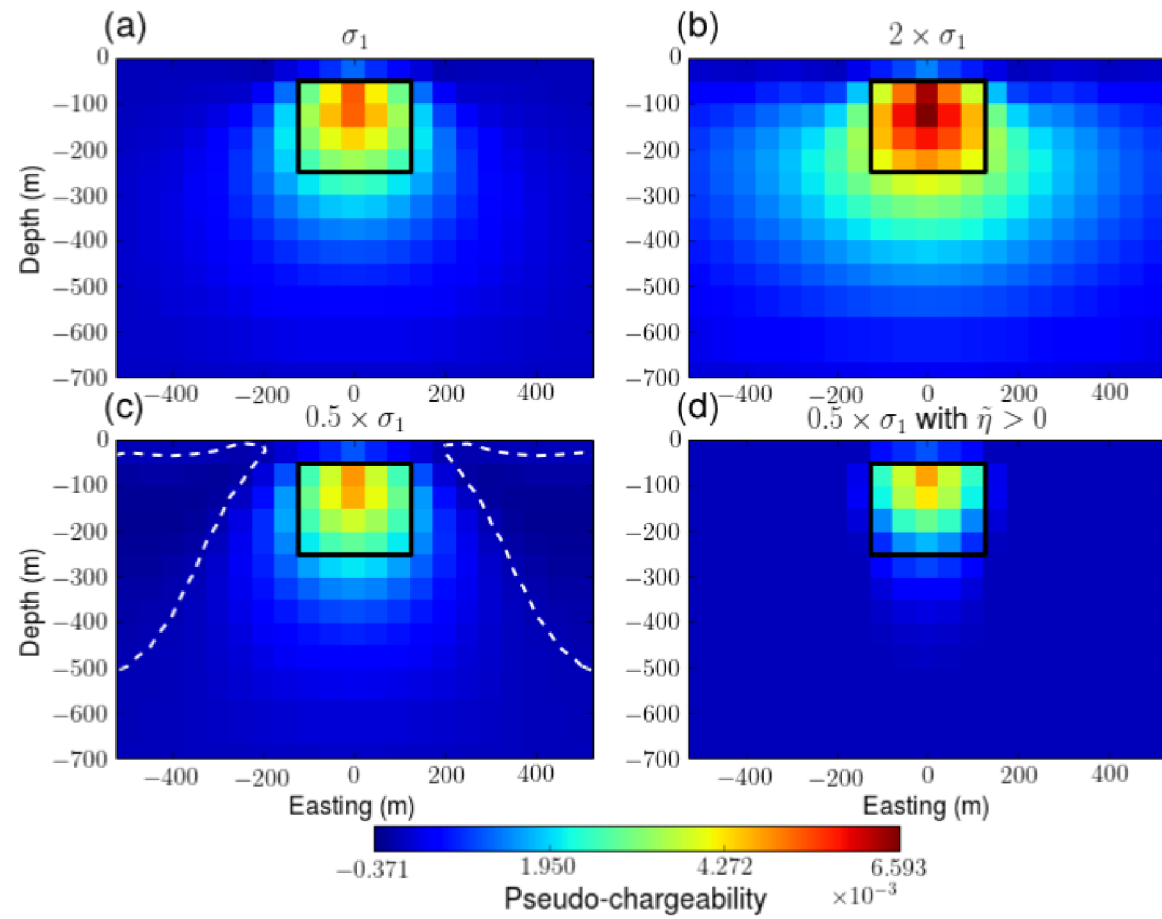


Figure 17. Effect of depth weight in 3D IP inversion. (a) True pseudo-chargeability model on vertical section at 0 m-northing. Recovered pseudo-chargeability models (b) without depth weight and (c) with depth weight.



**Figure 18.** IP responses on a profile line at 0 m-northing. IP responses are computed from perturbed  $\sigma_\infty$  models. Half-space conductivity ( $\sigma_1$ ) is perturbed two times higher or less resulting in overestimated (dotted line) and underestimated (dashed line) IP responses. Solid line shows the true IP response.

44 Seogi Kang and Douglas W. Oldenburg



**Figure 19.** Recovered pseudo-chargeability sections from 3D IP inversions at 0 m-northing. (a)  $d^{IP}$  with true  $\sigma_1$ . (b)  $d^{IP}$  with  $2 \times \sigma_1$ . (c)  $d^{IP}$  with  $0.5 \times \sigma_1$ . (d)  $d^{IP}$  with  $0.5 \times \sigma_1$  and the positivity constraint on the pseudo-chargeability. White dashed lines contour zero-crossing lines.

## On recovering distributed IP information from inductive source time domain electromagnetic data 45

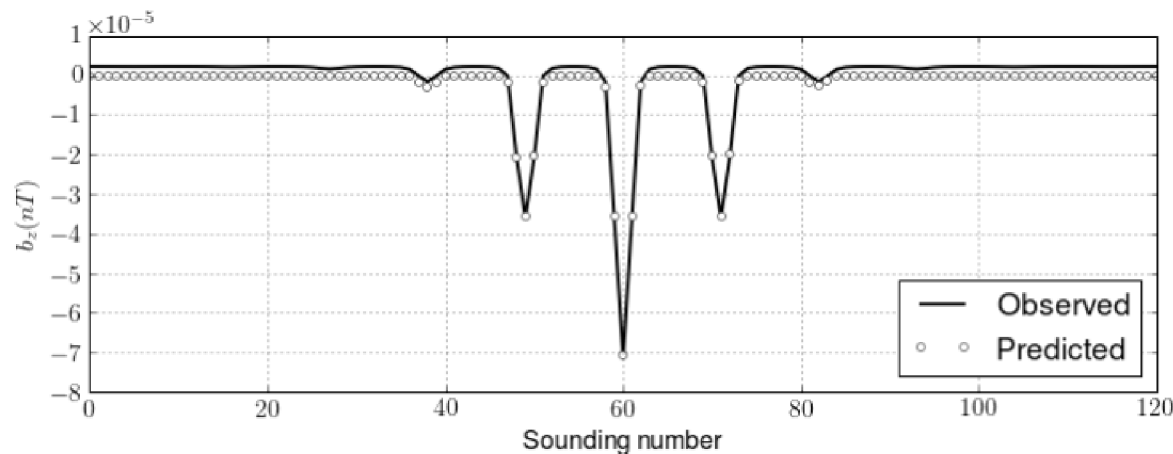


**Figure 20.** Comparison of the observed (solid line) and predicted (empty circles) data.  $d^{IP}$  response was generated with underestimated half-space conductivity ( $0.5 \times \sigma_1$ ). The positivity constraint was used in the 3D IP inversion.

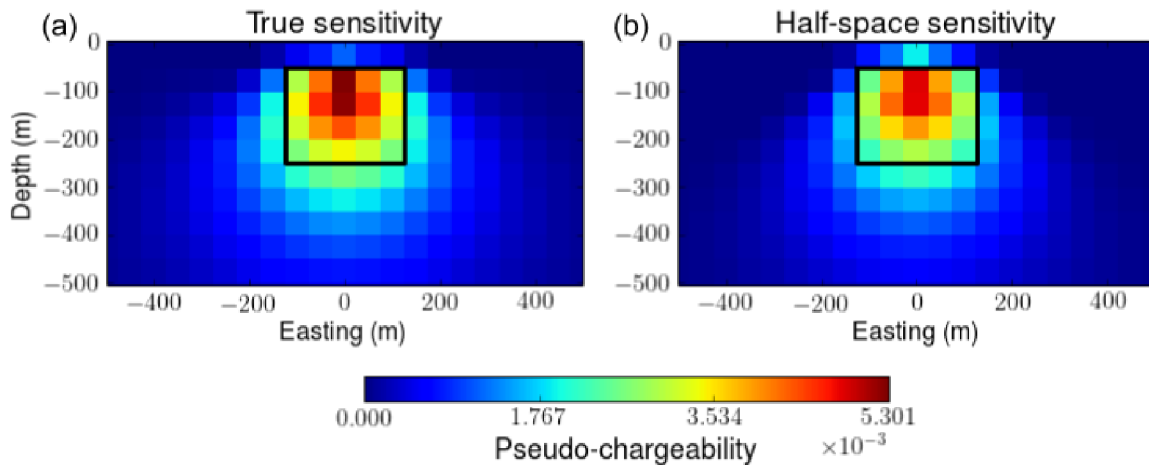
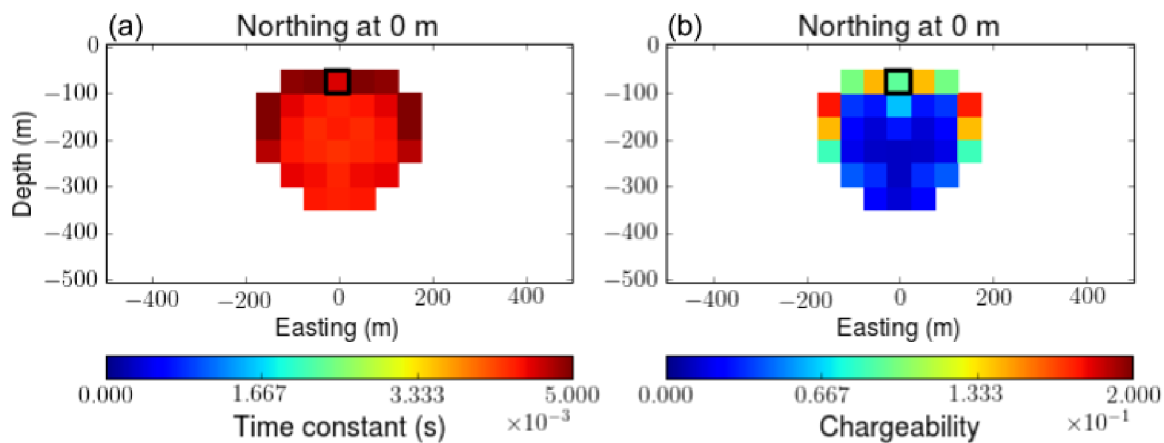
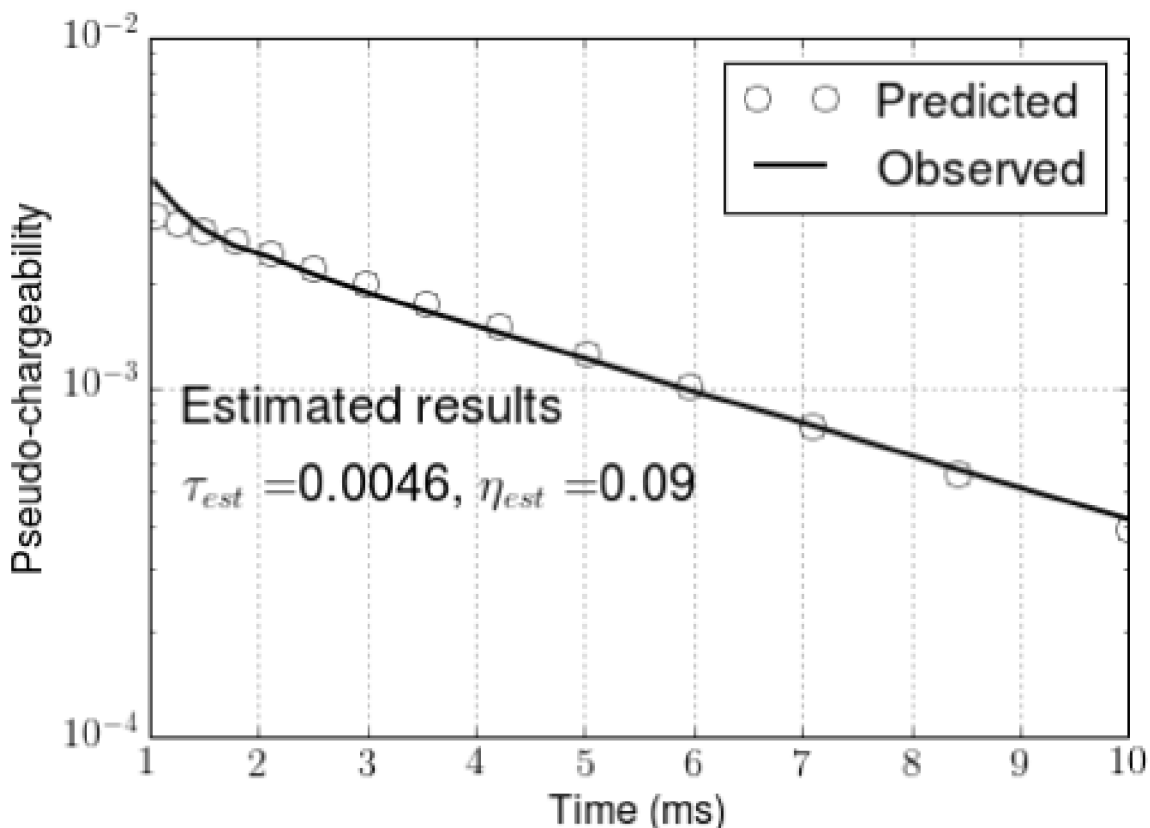


**Figure 21.** Recovered pseudo-chargeability sections from the 3D IP inversions at 0 m-northing. (a) True and (b) incorrect  $\sigma_\infty$  is used to compute sensitivity function. For the incorrect sensitivity we used half-space conductivity ( $\sigma_1$ ).

1  
2  
3 46 Seogi Kang and Douglas W. Oldenburg  
5  
6  
7  
8  
9  
10  
11  
12  
13  
14  
15  
16  
17  
18  
19  
20  
21



22 Figure 22. Section views of recovered (a) time constant and (b) chargeability. Any region where the pseudo-  
23 chargeability shown in Fig. 21a is smaller than 0.001 is ignored this analysis, and blanked.  
24  
25  
26  
27  
28  
29  
30  
31  
32  
33  
34  
35  
36  
37  
38  
39  
40  
41  
42  
43  
44  
45  
46  
47  
48  
49  
50  
51  
52  
53  
54



55 Figure 23. Comparisons of the observed and predicted pseudo-chargeability at a single pixel in a chargeable  
56 body. Empty circles and solid line indicate predicted and observed pseudo-chargeability, respectively. Estimated  
57 time constant and chargeability are expressed as  $\tau_{est}$  and  $\eta_{est}$ , respectively.  
58  
59  
60

1  
2  
3      *On recovering distributed IP information from inductive source time domain electromagnetic data*    47  
4  
5

6      **APPENDIX A: DISCRETIZATION OF STEADY-STATE MAXWELL'S EQUATIONS**  
7  
8

9      As shown in eq. (31), computation of our linearized kernel requires solving steady-state Maxwell's  
10 equations. We discretize this system using a mimetic finite volume (FV) method with weak formulation  
11 (Yee 1966; Haber 2014). For the discretization, we assume that the electric field  $\vec{e}$  is discretized by  
12 grid function  $e$  on cell edges and magnetic flux density  $\vec{b}$  is discretized by grid function  $b$  on cell faces.  
13 The electrical potential  $\phi$  is discretized by a grid function  $\phi$  on cell nodes. For a clear representation  
14 of the derivation, recall Maxwell's equations in steady state as  
15  
16

17       $\vec{j} = \sigma_\infty \vec{e} = -\sigma_\infty \vec{\nabla} \phi, \quad (A.1)$   
18  
19

20       $-\nabla \cdot \vec{j} = \nabla \cdot \vec{j}_s, \quad (A.2)$   
21  
22

23       $\vec{j}|_{\partial\Omega} \cdot \hat{n} = 0, \quad (A.3)$   
24

25      where  $\partial\Omega$  indicates boundary surface of the system and  $\hat{n}$  is the normal vector of the boundary surface.  
26  
27      The weak form of those eqs can be written as

28       $(\vec{j}, \vec{w}) + (\sigma_\infty \vec{\nabla} \phi, \vec{w}) = 0, \quad (A.4)$   
29  
30

31       $-(\vec{j}, \vec{\nabla} \psi) = (\vec{j}_s, \vec{\nabla} \psi). \quad (A.5)$   
32  
33

34      The inner products  $(\vec{j}, \vec{w})$ ,  $(\sigma_\infty \vec{\nabla} \phi, \vec{w})$ ,  $(\vec{j}, \vec{\nabla} \psi)$  and  $(\vec{j}_s, \vec{\nabla} \psi)$  are edge based products. Here we define  
35  
36      the inner product as

37       $(\vec{a}, \vec{b}) = \int_\Omega \vec{a} \cdot \vec{b} dv, \quad (A.6)$   
38  
39

40      where  $\Omega$  is the volume of the system. By discretizing  $\vec{\nabla}$  operator and the inner product in space, we  
41  
42      obtain

43       $\mathbf{M}^e \mathbf{j} + \mathbf{M}_{\sigma_\infty}^e \mathbf{G} \phi = 0, \quad (A.7)$   
44  
45

46       $-\mathbf{G}^T \mathbf{M}^e \mathbf{j} = \mathbf{G}^T \mathbf{M}^e \mathbf{j}_s, \quad (A.8)$   
47  
48

49      where  $\mathbf{M}^e$  performs volume averaging, and  $\mathbf{M}_{\sigma_\infty}^e$  is the mass matrix of conductivity ( $\sigma_\infty$ ), which  
50  
51      discretizes the edge based inner product. Further details on the formation of this matrix see Haber  
52  
53      (2014).

54      By substituting eq. (A.7) to (A.8), we have  
55  
56

57       $\mathbf{A}_{\sigma_\infty} \phi = \mathbf{rhs}^{DC}, \quad (A.9)$   
58  
59

60      where  $\mathbf{A}_{\sigma_\infty} = \mathbf{G}^T \mathbf{M}_{\sigma_\infty}^e \mathbf{G}$  and  $\mathbf{rhs}^{DC} = \mathbf{G}^T \mathbf{M}^e \mathbf{j}_s$ . We use SIMPEG's tensor mesh and solver  
61  
62      classes to form and solve above linear system (Cockett et al. 2015).

1  
2  
3 48 Seogi Kang and Douglas W. Oldenburg  
4  
5

1 APPENDIX B: DISCRETIZATION OF THE LINEARIZED KERNEL  
2  
3

4 To obtain a linear form of equation shown in eq. (37), we first discretize Biot-Savart law shown in  
5 eqs (35) and (36). In our discretization  $\vec{j}^{IP}$  and  $\tilde{\eta}$  are defined on the cell centers, and those for each  
6 time channel are constant in a cell volume, whereas  $\vec{e}^{ref}$  is defined on the cell edges. We define the  
7 number of cells and edges in 3D space as  $nC$  and  $nE$ , respectively. The discretized IP current density,  
8  $\mathbf{j}_{cc}^{IP} \in \mathbb{R}_1^{3nC}$ , is defined at the cell center. Since  $\vec{j}^{IP}$  has three components, we first discretize the  
9 integration operator including cross product ( $\int_v \frac{\times \hat{r}}{r^2} dv$ ) as  
10  
11

$$\mathbf{G}_{Biot} = \begin{bmatrix} \mathbf{e}^T & \mathbf{0} & \mathbf{0} \\ \mathbf{0} & \mathbf{e}^T & \mathbf{0} \\ \mathbf{0} & \mathbf{0} & \mathbf{e}^T \end{bmatrix} \begin{bmatrix} \mathbf{0} & \mathbf{S}_z & -\mathbf{S}_y \\ -\mathbf{S}_z & \mathbf{0} & \mathbf{S}_x \\ \mathbf{S}_y & -\mathbf{S}_x & \mathbf{0} \end{bmatrix}, \quad (B.1)$$

12 where  
13  
14

$$\mathbf{S}_l = \text{diag}(\mathbf{v} \oplus \mathbf{r}_l \oplus \frac{1}{\mathbf{r}^2}), \quad l = x, y, z$$

15 and the electric field,  $\mathbf{e} \in \mathbb{R}_1^{nE}$  is a column vector,  $\text{diag}(\cdot)$  is the diagonal matrix and  $\oplus$  is the  
16 Hadamard product. Then we discretize  $\vec{j}^{IP}$  shown in eq. (33) as  
17  
18

$$\mathbf{j}_{cc}^{IP}(t) = \mathbf{S} \text{diag}(\mathbf{e}_{max}^F) \mathbf{A}_c^{eT} \text{diag}(\mathbf{v}) \text{diag}(\sigma_\infty) \tilde{\eta}(t), \quad (B.2)$$

19 where  $\mathbf{A}_c^e$  is discrete averaging matrix from edge to cell center and  
20  
21

$$\mathbf{S} = \mathbf{A}_{ccv}^e \mathbf{M}^{e-1} [\mathbf{M}_{\sigma_\infty}^e \mathbf{G} \mathbf{A}_{\sigma_\infty}^{-1} \mathbf{G}^T - \mathbf{I}] \text{diag}(\mathbf{e}_{max}^F) \mathbf{A}_c^{eT} \text{diag}(\mathbf{v}) \text{diag}(\sigma_\infty). \quad (B.3)$$

22 Here  $\mathbf{A}_{ccv}^e$  is discrete averaging matrix from edge to cell center with consideration of three component  
23 vector:  $\in \mathbb{R}_{nE}^{3nC}$ . Thus, we can have a linear equation for a single time channel as  
24  
25

$$\mathbf{b}^{IP} = \mathbf{G}_{Biot} \mathbf{S} \tilde{\eta},$$

26 Finally, by letting  
27  
28

$$\mathbf{J} = \mathbf{G}_{Biot} \mathbf{S}, \quad (B.4)$$

29 we have  
30  
31

$$\mathbf{b}^{IP} = \mathbf{J} \tilde{\eta}, \quad (B.5)$$

32 where  $\mathbf{J}$  is the Jacobian matrix of the linear equation, and since  $\mathbf{J}$  is static, we also obtain  
33  
34

$$-\frac{\partial \mathbf{b}^{IP}}{\partial t} \Big| = \mathbf{J} \left( -\frac{\partial \tilde{\eta}}{\partial t} \Big| \right). \quad (B.6)$$